Cleaner production of methanol from carbon dioxide over copper and iron supported MCM-41 catalysts using innovative integrated magnetic field-packed bed reactor

Sirapassorn Kiatphuengporn [a,b], Waleeporn Donphai [a,b], Pongsakorn Jantaratana [c], Nevzat Yigit [d], Karin Föttinger [d], Günther Rupprechter [d], and Metta Chareonpanich [a,b,*]

[a] *KU-Green Catalysts Group, Department of Chemical Engineering, Faculty of Engineering, Kasetsart University, Bangkok 10900, Thailand*

[b] *NANOTEC Center for Nanoscale Materials Design for Green Nanotechnology and Center for Advanced Studies in Nanotechnology and its Applications in Chemical, Food and Agricultural Industries, Kasetsart University, Bangkok 10900, Thailand*

[c] *Department of Physics, Faculty of Science, Kasetsart University, Bangkok 10900, Thailand*

[d] *Institute of Materials Chemistry, Vienna University of Technology, Getreidemarkt 9/BC/01, Vienna 1060, Austria*

Highlights

- External magnetic field was equipped to a conventional catalytic fixed-bed reactor.
- Methanol was produced via CO_2 hydrogenation over *w*(Cu)-*w*(Fe)/MCM-41 catalysts.
- This integrated magnetic field reactor promoted methanol production at lower temp.
- The operating temperature could be reduced up to 57.7 ^oC at the same rate of reaction.
- Less CO_2 emissions by means of temperature saving was obtained from this process.

* Corresponding author. Tel.: +66 2797 0999 ext. 1215; Fax: +66 2561 4621.

E-mail address: fengmtc@ku.ac.th (M. Chareonpanich)

Abstract

In this research, an external magnetic field has been employed to a catalytic packed bed reactor in order to improve the performance of copper and iron supported MCM-41 catalysts in carbon dioxide utilization through hydrogenation reaction. The result showed that magnetic field significantly improved carbon dioxide conversion at all reaction temperatures. The highest carbon dioxide conversion was obtained over 10(Cu)-10(Fe)/MCM-41 catalyst with magnetic flux density of −27.7 mT in north-to-south (N–S) direction which was 1.8 times higher than that of without magnetic field. In addition, the methanol space time yield was 1.5 times higher than that of without magnetic field and therefore, the lowest apparent activation energy (34.5 kJ/mol) was achieved. As a result, this integrated magnetic field-packed bed reactor could significantly reduce the operating temperature by 32.9 ºC, 33.8 ºC, and 57.7 ºC over 10(Cu)/MCM-41, 10(Fe)/MCM-41, and 10(Fe)-10(Cu)/MCM-41 catalysts, respectively compared to those without magnetic field at the reaction temperature of 260 ºC. With 10(Fe)-10(Cu)/MCM-41 catalyst, magnetic field could save electric energy costs of 2,074–48,373 $/a with payback periods of 4.7–0.2 a at reaction temperatures of 180–260 ºC, respectively based on CO_2 conversion of 100 kg/h. This outstanding performance could be attributed to the fact that magnetic field facilitated carbon dioxide adsorption on the magnetized catalyst surfaces. This led to the advantages of a heterogeneously catalyzed reaction including the enhancement of carbon dioxide utilization and methanol formation, the decrease of operating temperature, and the simultaneous decrease of carbon dioxide emission by means of energy-efficient process modification.

Keywords: Sustainable innovation; CO_2 utilization; Methanol; Hydrogenation; Magnetic field; Fe-Cu catalyst

1. Introduction

Over the past decades, the main factor causing global warming is the increase of carbon dioxide (CO_2) emission produced by human activities such as transportation, deforestation, and combustion of fossil fuels (Huisingh et al., 2015; Taghdisian et al., 2015). The utilization of CO_2 to produce value-added chemical feedstock, fuels, and alternative energy not only solves global warming and climate change problems, but also potentially provides a great opportunity for green sustainable development in energy and environment (Fernandez et al., 2016; Zhou et al., 2015). Among other technologies for CO_2 utilization, hydrogenation of CO_2 has received great attention as one of the effective ways to control and reduce CO_2 concentration in atmosphere (Yang et al., 2015; Van-Dal et al., 2013).

Due to the attractive economic value and broad industrial utilization, methanol is an important chemical that can be regarded as a fuel additive or clean fuel, hydrogen carrier, and feedstock (Luu et al., 2016; Yang et al., 2015). However, the main products of CO_2 hydrogenation are carbon monoxide (CO) and methane (CH_4), while low alcohols and dimethyl ether are produced (Ren et al., 2015; Riaz et al., 2013). In order to improve alcohol selectivity, many researchers have focused on the important factors, e.g., metal catalysts (Chinniyomphanich et al., 2016; Bonura et al., 2014), promoters (Angelo et al., 2015; Rafati et al., 2015), supports (Ren et al., 2015; Kiatphuengporn et al., 2014), catalyst preparation techniques (Romero-Sáez et al., 2016), and operating conditions (Riaz et al., 2013).

Concerning all the catalysts studied to date, copper-based catalysts are widely used for methanol synthesis (Bonura et al., 2014; Arena et al., 2013; Zhan et al., 2014). However, the major competitive pathway is the reverse water-gas shift (RWGS) reaction which selectively

produces CO. For the hydrogenation of CO to hydrocarbons, the catalysts, e.g., iron (Fe), cobalt (Co), nickel (Ni) and ruthenium (Ru) have been used (Mohsenzadeh et al., 2016; Torshizi et al., 2015). Regarding a choice of catalysts, Fe is one of the most active metal catalysts that can improve CO conversion and enhance selectivity to alcohols or higher hydrocarbons through Fischer-Tropsch synthesis (FTS) reaction (Zhang et al., 2015; Rafati et al., 2015). In order to modify the catalyst for alcohols and hydrocarbons production, it could be expected that Fe-Cu catalysts are the most promising choice as they are cheap, active and selective to desired products. Furthermore, Mobil Composition of Matter No. 41 (MCM-41), one of the mesoporous silica materials, is a good choice to use as a catalyst support in order to increase the probability for surface reaction regarding its long-range, ordered hexagonal structure (Fig. 1, Supplementary information), and high surface area (Jiang et al., 2015; Kiatphuengporn et al., 2014). However, Fe-Cu supported MCM-41 catalysts still have low efficiencies for converting CO_2 compared to Cu/ZnO-ZrO_2 catalysts (Ren et al., 2015; Bonura et al., 2014; Arena et al., 2013).

With an attempt to improve both economic and environmental aspects towards the cleaner production, an external magnetic field is of great potential application in selective alcohol production through CO_2 hydrogenation due to its advantages in convenient use, low running cost, non-toxic, no secondary pollution, and wide application range. In the recent literature, magnetic field was used in many applications such as wastewater treatment for high algal growth and oxygen production (Tu et al., 2015), separation and purification process for recovery and removal of magnetic components (Zheng et al., 2015; Zou et al., 2015), solidification and crystallization process to control chemical structures and function of materials (Radhakrishnan et al., 2015; Onodera et al., 2014), and photocatalytic reaction to increase reaction rates and product yields (Okumura et al., 2015; Udagawa et al., 2011).

Up to date, very little research exploring the effect of magnetic field on catalytic CO_2 hydrogenation reactions, particularly in a packed bed reactor, have been reported.

Accordingly, in this research, the investigation in the area of green and innovative production regarding the effect of magnetic field on CO_2 utilization for methanol production through catalytic hydrogenation process was focused. The reaction over Fe-Cu/MCM-41 catalysts was carried out in an integrated magnetic field-packed bed reactor, and the results were compared to that one without magnetic field. We found that magnetic field could significantly increase the performance of Fe-Cu supported MCM-41 catalysts with intrinsic magnetic property, and facilitate the energy-efficient process with lower CO_2 emission and less energy consumption by means of lowering the operating temperature while maintaining the rate of CO_2 conversion.

2. Experimental

2.1. Synthesis of w(Fe)-w(Cu)/MCM-41 catalysts with intrinsic magnetic property

MCM-41 support was synthesized through a sol-gel method using tetraethyl orthosilicate (TEOS) as a silica source and cetyltrimethyl ammonium bromide (CTAB) as a template following Kiatphuengporn et al. (2014). Briefly, 1.21 g CTAB was dissolved in 48 ml deionized water, followed by adding 3.71 ml TEOS and 0.5 ml ammonium hydroxide solution (NH_4OH) into CTAB solution. The molar composition of the gel mixture was 1.0 TEOS: 0.2 CTAB: 160 H_2O: 1.5 NH_3. After stirring at 50 ^oC for 24 h, the resulting gel was hydrothermally heated in a Teflon-lined autoclave at 100 ^oC for 24 h. Then, the solid product was filtered, washed with deionized water, dried at 100 ^oC overnight, and calcined in air at 550 ^oC for 4 h with a heating rate of 4 ^oC/min. The mesoporous silica MCM-41 support was obtained.

The catalysts with different mass fractions of Fe and Cu (0 % and 10 %) loaded on MCM-41 support were prepared by incipient wetness impregnation method. Certain weights of both iron nitrate nonahydrate ($Fe(NO_3)_3 \cdot 9H_2O$) and copper nitrate trihydrate

($Cu(NO_3)_2 \cdot 3H_2O$) were completely dissolved in deionized water and dropped into 1 g of MCM-41 support under stirring at room temperature for 1 h. The obtained mixture was dried with microwave at 800 W for 1 min, and then calcined in air at 550 ^oC for 4 h. The obtained catalysts were denoted as *w*(Fe)-*w*(Cu)/MCM-41, where *w* was mass fractions of Fe and Cu loading.

2.2. Physicochemical and CO_2 adsorption capacity of w(Fe)-w(Cu)/MCM-41 catalysts

The textural properties of MCM-41 support and *w*(Fe)-*w*(Cu)/MCM-41 catalysts were analyzed by using nitrogen sorption equipment (Quantachrome Corporation, Autosorb-1C instrument). Prior to each measurement, the sample was degassed at 200 ^oC for 12 h. The specific surface area of the catalysts was examined by using the Brunauer-Emmett-Teller (BET) analysis in a relative pressure (p/p_0) range between 0.05 and 0.95, where the specific pore volume was measured at a relative pressure of 0.995. Pore size distribution was calculated by using Barrett-Joyner-Halenda (BJH) method.

The crystalline phases of catalysts before and after reduction process were investigated by X-ray diffraction (XRD: Bruker D8 Advance) operating under an electric tension of 40 kV and a current of 40 mA in the diffraction angle (2θ) range of 10–80 ^{o}. Iron and copper oxide crystallite sizes were calculated by the Scherrer equation.

Morphology and structure of catalysts were examined by using high-resolution transmission electron microscopy (HR-TEM: JEOL JEM-2000 EX II) with the acceleration electric tension of 200 kV. The samples were prepared by suspending in ethanol and then dispersing on holey carbon-coated grids.

The acidity and CO_2 adsorption capacity of catalysts were investigated by a temperature-programmed desorption (TPD) of NH_3 and CO_2, respectively. Prior to each measurement, 50 mg of catalyst was placed in a quartz tube reactor and then the reactor was evacuated by a diffusion pump (base pressure, 0.5 mbar). The sample was pretreated with

oxygen (O_2) at 550 ^oC with a heating rate of 5 ^oC/min during 1 h and then reduced with H_2 (100 mbar) at 550 ^oC for 1 h. After that, the sample was evacuated and cooled down to 100 ^oC for NH_3 adsorption and room temperature for CO_2 adsorption. NH_3 or CO_2 (100 mbar) was fed into the reactor for 1 h. Then, the sample was evacuated until a constant signal was obtained. The experiment was carried out in the temperature range of 25–550 ^oC with a heating rate of 5 ^oC/min. The adsorbed NH_3 or CO_2 was desorbed by heating the reactor from adsorption temperature to 550 ^oC with a heating rate of 5 ^oC/min. A continuous mass spectrometer (Balzers Prisma 260) was used to simultaneously analyze the desorbed NH_3 or CO_2 at mass-to-charge ratio (*m/z*) signal of 16 and 44.

2.3. The reducibility and magnetic properties of w(Fe)-w(Cu)/MCM-41 catalysts

The reducibility of catalysts was examined by the temperature-programmed reduction (TPR) measurements performed in a continuous flow apparatus using an inconel tube reactor (inconel-600, d_o = 9.5 mm). In each TPR experiment, 0.2 g of catalyst was heated in a flow of gas mixture of hydrogen (H_2) and argon (Ar) ($\phi(H_2)$ = 9.6 %, balanced in Ar) at 15 ml/min. The experiment was carried out in the range of 25–1000 ^oC with a heating rate of 5 ^oC/min. The hydrogen gas consumption was monitored by using Shimadzu gas chromatograph (GC-2014) equipped with a thermal conductivity detector (TCD).

The local geometry changes of Fe species in catalysts during reduction stage with hydrogen gas at 25–480 ^oC, and holding stage at 480 ^oC for 3 h were investigated by time-resolved x-ray absorption spectroscopy (TRXAS) at Beamline 2.2 of the SLRI, Thailand. XANES spectra of Fe K-edge were collected in the energy range of 6975–7525 eV in the transmission detection mode using ionization chamber.

The magnetic properties of catalysts before and after reduction process were measured by using a vibrating sample magnetometer (VSM) with a hall probe-based gaussmeter (Lakeshore 7404) at room temperature under an external magnetic field up to 796 kA/m. The

coercive field and the remanent magnetization were determined from the interception of magnetic hysteresis loop on the *x* and *y* axis, respectively.

2.4. Effect of magnetic field on performances of w(Fe)-w(Cu)/MCM-41 catalysts

The performances of *w*(Fe)-*w*(Cu)/MCM-41 catalysts for CO_2 hydrogenation reaction were carried out in a magnetic field-assisted, continuous-flow packed bed reactor system (in Fig. 1). A ring cast Alnico permanent magnet (Bunting Magnetics Co., Ltd.: d_o = 25.4 mm; d_i = 19.0 mm; τ = 12.7 mm; grade 5), with curie and maximum operating temperatures of 840 ^oC and 538 ^oC, respectively assembled with the stainless steel reactor (SUS-316, d_o = 9.5 mm) was used to generate an external magnetic field. Magnetic field orientations (north-to-south (N–S) and south-to-north (S–N) alignments) and magnetic flux density at the catalyst bed (±20.8 mT and ±27.7 mT) could be controlled by switching magnetic poles and varying numbers of magnet pairs (2 pairs and 4 pairs), respectively. The magnetic flux densities within the reactor were measured before and after each catalytic reaction test in both radial (every 3 mm from the center of reactor) and axial (every 0.5 mm from the left side to right side of reactor) directions by using magnetometer at room temperature. The flux densities were almost similar to those before reaction. The example of measurement in the case of 4 pairs of magnet is shown in Table 1, Supplementary information. The magnetic flux densities in radial direction were almost not changed, while those in axial direction were different (as shown in Fig. 1). The error of magnetic flux density in radial direction is in between ±1.0 % and the sensitivity of magnetometer is ±5 % of reading. In addition, the magnetic flux density of the earth ranges of 0.025–0.065 mT depending on the geographic position on earth which was approximately 1,000 times lower than the magnetic flux density in this study. Therefore, the effect of the earth's magnetic field on the experimental result can be negligible. Fig. 1 exhibits the gradients of magnetic flux density (color band: green, –; red, +) in the case of two

pairs and four pairs of magnets with N−S alignment. At the center of catalyst bed, the highest magnetic flux density with the minus sign (an opposite direction with respect to inlet gas flow rate) were observed (green color: −20.8 mT and −27.7 mT for two pairs and four pairs of magnets, respectively). On the other hand, with S−N alignment the highest magnetic flux density with the plus sign (a similar direction with respect to inlet gas flow rate) were obtained (red color: +20.8 mT and +27.7 mT). Before the reaction, 0.2 g of catalyst was packed in the reactor at a position centered between the magnet pairs. After that, the catalyst was activated by using oxygen (a flow rate of 30 ml/min) at 550 ^{o}C for 1 h and then reduced in situ with hydrogen (a flow rate of 60 ml/min) at 480 ^{o}C for 3 h. After catalyst activation, the reactor was cooled down to room temperature and reactant gases (CO_2 and H_2 with molar ratio of 1:3) were introduced into the system with space velocity (*s*) of 16,300 h^{-1}. The space velocity is generally calculated by using Equation (1) as follows:

$$s = \frac{v_{\text{total}}}{V_{\text{R}}} \tag{1}$$

where v_{total} is the volumetric flow rate of total reactant gases and V_{R} is the reactor volume.

The reaction was performed at temperature range of 180–260 ^{o}C and total pressure of 10 bar. The activity data were recorded and reported as an average value after the reaction reached its steady state with time-on-steam of approximately 1 h per each reaction temperature. The obtained products were analyzed by gas chromatograph (Shimadzu, GC-2014) equipped with a thermal conductivity detector (TCD) for H_2, CO, CO_2, and CH_4 analysis using Unibead-C packed column and argon (>99.9 % purity) as the carrier gas, and Shimadzu GC-8A with flame ionization detector (FID) for C_1–C_4 hydrocarbons analysis using a Porapak-Q packed column. For the latter, helium (99.995 % purity) was used as the carrier gas, while H_2 and air were used as the combustion gas for flame ionization detection.

The activities of *w*(Fe)-*w*(Cu)/MCM-41 catalysts with different magnetic field orientations and magnetic flux density were evaluated in terms of fractional conversion of

CO_2 and products distribution, and compared to that one without magnetic field. The fractional conversion of CO_2 (X_{CO_2}) was calculated by using Equation (2) as follows:

$$X_{CO_2}\,(\%) = \left(\frac{[n_{CO_2}]_{in} - [n_{CO_2}]_{out}}{[n_{CO_2}]_{in}}\right) \times 100 \quad (2)$$

where n_{CO2} is moles CO_2. In addition, the apparent activation energies, temperature saving by mean of operating temperature, CO_2 consumption and economic evaluation by mean of the electric energy saving cost and payback period were calculated and reported.

3. Results and discussion

3.1. Textural and chemical property of MCM-41 support and w(Fe)-w(Cu)/MCM-41 catalysts

Nitrogen adsorption-desorption isotherms and pore size distribution of MCM-41 support and *w*(Fe)-*w*(Cu)/MCM-41 catalysts are shown in Fig. 2, and the specific surface area, specific pore volume, and average pore size are listed in Table 1. In Fig. 2A, MCM-41 support and *w*(Fe)-*w*(Cu)/MCM-41 catalysts exhibited type IV isotherm with H1 hysteresis loop (according to IUPAC classification (Alothman et al., 2012)), indicating the characteristic of capillary condensation with in uniform mesoporous structures (Li et al., 2012; Wang et al., 2012). From Fig. 2B and Table 1, MCM-41 support displayed bimodal pore structure which pore sizes of 2.7 nm and 30.5 nm. For 10(Fe)/MCM-41 catalyst, the pore sizes were almost similar to those of MCM-41 support, while the larger pore size of Cu containing catalysts both 10(Cu)/MCM-41 and 10(Fe)-10(Cu)/MCM-41 was decreased from 30.5 nm to 17.5 nm and 17.2 nm, respectively. The decrease of the larger pore size, specific surface area and specific pore volume might occur due to the loaded metals partially blocked and entered into mesopores of MCM-41 support during the impregnation process (Chinniyomphanich et al., 2016; Jiang et al., 2015).

The crystalline structures of *w*(Fe)-*w*(Cu)/MCM-41 catalysts before and after reduction process were characterized by using XRD technique, and the diffraction patterns are shown in Fig. 3. The average CuO and Fe_2O_3 crystallite sizes were determined by the Scherrer equation and summarized in Table 1. The diffraction patterns of calcined 10(Cu)/MCM-41 and 10(Fe)/MCM-41 catalysts corresponded to monoclinic CuO and cubic crystalline Fe_2O_3 phases (Zhou et al., 2015; Zhang et al., 2010) with the crystallite sizes of 20.4 nm and 16.7 nm, respectively. For calcined 10(Fe)-10(Cu)/MCM-41 catalyst, both CuO and Fe_2O_3 phases were observed with the crystallite sizes of 19.6 nm and 31.3 nm, respectively. It was found from this result that the incorporated Cu with Fe led to the agglomeration of Fe_2O_3 particles as evidenced by the larger crystallite size in comparison to those of calcined 10(Fe)/MCM-41 catalysts. The crystalline phases of catalysts after reduction process will be discussed in the next section.

In order to examine the morphology and metal particle sizes of *w*(Fe)-*w*(Cu)/MCM-41 catalysts, TEM measurement was performed as the images shown in Fig. 4. It was observed that CuO and Fe_2O_3 particles of 10(Cu)/MCM-41 and 10(Fe)/MCM-41 catalysts were in nano-size range and well-dispersed on the support. The average CuO and Fe_2O_3 particle sizes (Fig. 2, Supplementary information) were 24.3 nm and 3.9 nm for 10(Cu)/MCM-41 and 10(Fe)/MCM-41 catalysts, respectively; these were not consistent with the XRD result of Fe_2O_3 crystallite sizes (16.7 nm, in Table 1), suggesting that the crystallite size obtained by XRD technique contained several primary crystallite grains which lead to a larger crystallite size than that of TEM technique (Hyde et al., 2008). For 10(Fe)-10(Cu)/MCM-41 catalyst, the agglomeration of metal particles was observed. In order to further identify the dispersion of each element, the same area of 10(Fe)-10(Cu)/MCM-41 catalyst (Fig. 4c) was scanned by the mapping technique of energy-dispersive X-ray spectroscopy in scanning transmission electron microscopy mode (STEM/EDS). The result revealed that CuO particles were finely dispersed (Fig. 4d), while an agglomeration of Fe_2O_3 particles was observed (Fig. 4e) which was in

good agreement to Fe_2O_3 crystallite size from XRD technique (31.3 nm). It was suggested that the higher mass fraction of metal loading and the incorporation of Cu with Fe could enhance metal agglomeration, leading to the increase of metal particle sizes.

3.2. Reducibility, magnetic property and CO_2 adsorption ability of w(Fe)-w(Cu)/MCM-41 catalysts

In order to examine the type and reduction behavior of Fe and Cu oxide species, H_2-TPR experiment was performed and the corresponding reduction profiles are shown in Fig. 5. It was found that all catalysts exhibited different reduction behavior. Regarding the XRD result (Fig. 3), oxide forms of copper and iron were clearly observed in the catalyst. Accordingly, 10(Cu)/MCM-41 catalyst (Fig. 5a) showed a broad reduction peak with its maximum at 262 ^oC, corresponding to the reduction of CuO to Cu^0. For 10(Fe)/MCM-41 catalyst in Fig. 5b, the reduction profile could be deconvoluted into four peaks which were ascribed to three stepwise reductions of iron oxide species to Fe^0 ($Fe_2O_3 \rightarrow Fe_3O_4 \rightarrow FeO \rightarrow Fe^0$), as was reported by Romero-Sáez et al. (2016) and Suo et al. (2012). Hematite (Fe_2O_3) was reduced to magnetite (Fe_3O_4) and then transformed to wüstite (FeO) at reduction temperature range of 200–500 ^oC. Thereafter, wüstite (FeO) was reduced to metallic iron (α-Fe or Fe^0) at 892 ^oC. In the case of 10(Fe)-10(Cu)/MCM-41 in Fig. 5c, the reduction profile was fitted into two reduction regions. The first region, at 262 ^oC, was similar to 10(Cu)/MCM-41 catalyst assigned to the reduction of CuO to Cu^0, while the second region in the temperature range of 350–650 ^oC was attributed to the reduction of Fe oxide species to Fe^0. It can be noted that the incorporation of Fe with Cu significantly enhanced the reducibility of iron oxides and decreased the reduction temperature of Fe oxide species as well (Bao et al., 2012; Zhang et al., 2010). Due to the operating temperature limitation of Alnico magnet, the reduction temperature of *w*(Fe)-*w*(Cu)/MCM-41 catalysts was therefore fixed as 480 ^oC.

The crystalline phases present in *w*(Fe)-*w*(Cu)/MCM-41 catalysts under the reduction condition at 480 ^{o}C for 3 h was further investigated and the results are shown in Fig. 3. The diffraction peaks of metal oxide species on *w*(Fe)-*w*(Cu)/MCM-41 catalysts were disappeared after reduction process. This evidently confirmed that upon reduction process, the crystalline phases of CuO and Fe_3O_4 were reduced to Cu^0 and Fe^0 without any detection of oxide phases.

The in situ XANES measurements under the reduction condition were performed to further confirm the transformation of iron oxide species in *w*(Fe)-*w*(Cu)/MCM-41 catalysts. The normalized Fe K-edge absorption spectra together with an amplified inset, showing the spectra of iron oxide species and Fe foil standard, are displayed in Fig. 6. During the reduction process, the spectra of *w*(Fe)-*w*(Cu)/MCM-41 catalysts were changed due to phase transformation. The compositions of Fe species analyzed from the corresponding spectra by linear combination fitting (LCF) analysis using the Athena program are summarized in Table 2. Before the reduction process, all calcined Fe containing catalysts exhibited three main phases of iron oxide species including *w*(Fe_2O_3) = 73.0 % and 81.6 %, *w*(Fe_3O_4) = 14.7 % and 24.7 %, and *w*(FeO) = 2.3 % and 3.7 %. However, after the reduction process, all the catalysts showed the mixed phases of iron oxide species and Fe^0, suggesting that iron oxide were partially transformed to Fe^0 and FeO. The mass fraction of Fe^0 over 10(Fe)/MCM-41 and 10(Fe)-10(Cu)/MCM-41 catalysts were 40.7 % and 45.6 %, respectively. It should be noted that both the metallic Fe and the amorphous iron oxide species were mainly formed, as were confirmed by XRD and LCF results.

In order to examine the magnetic property, *w*(Fe)-*w*(Cu)/MCM-41 catalysts before and after the reduction process were characterized by using a vibrating sample magnetometer (VSM). The magnetic hysteresis loops exhibited the information including saturation magnetization (M_s), remanence magnetization (M_r), and coercivity field (H_c) are shown in Fig. 7. Before the reduction process (Fig. 7a), small hysteresis loop near the zero field was observed on the calcined 10(Cu)/MCM-41 catalyst, while large hysteresis loop indicating

higher magnetic property was observed on the calcined 10(Fe)/MCM-41 catalyst. The order of saturation magnetization of the calcined catalysts was as follows: 10(Fe)/MCM-41 catalyst > 10(Fe)-10(Cu)/MCM-41 catalyst > 10(Cu)/MCM-41 catalyst.

After the reduction process (Fig. 7b), saturation magnetization, remanence, and coercivity field of *w*(Fe)-*w*(Cu)/MCM-41 catalysts significantly increased except those of reduced 10(Cu)/MCM-41 catalyst; a negative slope of magnetic hysteresis loop was observed due to diamagnetism. These results indicated that the magnetic property of reduced 10(Fe)/MCM-41 and 10(Fe)-10(Cu)/MCM-41 catalysts were enhanced due to the appearance of α-Fe phase (confirmed by XRD and LCF results). In addition, 10(Fe)-10(Cu)/MCM-41 catalyst exhibited the highest saturation magnetization, suggesting that the magnetic response of the sample increased with an increase of magnetic phase.

The CO_2-TPD was performed to investigate the strength of surface basic sites of *w*(Fe)-*w*(Cu)/MCM-41 catalysts (Fig. 8). The CO_2 desorption peaks at approximately 100 ^oC indicated the weakly-adsorbed CO_2 or bicarbonate species resulting from the interaction of CO_2 with basic hydroxyl groups. A broad peak at 200–500 ^oC revealed the strongly-adsorbed CO_2 on strong basic sites or a carbonate species (Ren et al., 2015; Phukan et al., 1999). The order of CO_2 adsorption capacity (Table 1) was: 10(Fe)-10(Cu)/MCM-41 (4.91) > 10(Fe)/MCM-41 (3.57) > 10(Cu)/MCM-41 (1.09) > MCM-41 (1.00). It was observed that the addition of Fe species significantly increased CO_2 adsorption capacity and the probability of CO_2 transformation to products. In addition, from the NH_3-TPD profiles (Fig. 3, Supplementary information), *w*(Fe)-*w*(Cu)/MCM-41 catalysts exhibited weak acid site at temperature lower than 250 ^oC which occurred from iron and copper species located in the framework (Wang et al., 2002), and medium acid site at the temperature range of 250–500 ^oC from the silanol groups on defective sites (Wang et al., 2002; Zhang et al., 2001). It should be noted that the acidity and basicity of catalysts vary depending on mass fractions of metal loading and the nature of the metals (Ajaikumar et al., 2009).

As a result, CO_2 adsorption on the magnetized *w*(Fe)-*w*(Cu)/MCM-41 surface with the magnetic field could be stronger than those of without magnetic field. This leads to the increase of catalyst performance both in CO_2 consumption and methanol production during CO_2 hydrogenation reaction.

3.3. Effect of magnetic field on performances of w(Fe)-w(Cu)/MCM-41 catalysts

Fig. 9 illustrates the catalytic performance in terms of CO_2 conversion and CH_3OH space time yield as a function of reaction temperature at different magnetic field direction and magnetic flux density. It was found that CO_2 conversion of all catalysts remarkably increased with increasing reaction temperature since CO_2 hydrogenation is endothermic reaction (Yang et al, 2015; Bonura et al, 2014).

Without magnetic field, the highest CO_2 conversions at 260 ^oC were 7.4 %, 6.6 %, and 8.7 % for 10(Cu)/MCM-41, 10(Fe)/MCM-41, and 10(Fe)-10(Cu)/MCM-41 catalysts, respectively. With the external magnetic field, CO_2 conversion was significantly enhanced and the highest conversions were 1.5 times, 1.3 times, and 1.8 times higher than those without magnetic field. Magnetic field orientation more strongly influenced the catalytic activity compared to the magnetic flux density. It was found that CO_2 conversion was notably increased at +20.8 mT in S–N direction over 10(Cu)/MCM-41 catalyst and at –27.7 mT in N–S direction over Fe containing catalysts. The effect of magnetic field orientation on CO_2 conversion was different over 10(Cu)/MCM-41 and Fe containing catalysts. This could be attributed to different magnetic natures of Fe and Cu species since 10(Cu)/MCM-41 catalyst exhibited diamagnetic property, while Fe containing catalysts showed ferri/ferromagnetic property, as shown in Fig. 7.

The influence of magnetic field on the activity in term of apparent activation energy (E_a) for CO_2 hydrogenation reaction over *w*(Fe)-*w*(Cu)/MCM-41 catalysts was investigated, and the results are tabulated in Table 3. The Arrhenius equation (Equation (3)) described the

relationship between the apparent activation energy and reaction temperature at constant hydrogen concentration (Riaz et al., 2013):

$$E_a = -R\frac{\mathrm{d}\ln k_a}{\mathrm{d}\frac{1}{T}} \quad (3)$$

where E_a is apparent activation energy (kJ/mol), R is gas constant (J/(mol K)), k_a is rate constant (1/sec), and T is reaction temperature (K). The slope of ln (k) versus 1/T (Fig. 4, Supplementary information) was used to calculate the activation energy. It was observed that the application of external magnetic field to the catalytic reaction system could significantly reduce the apparent activation energy. The lowest apparent activation energies over 10(Cu)/MCM-41, 10(Fe)/MCM-41, and 10(Fe)-10(Cu)/MCM-41 catalysts were 37.6 kJ/mol, 41.6 kJ/mol, and 34.5 kJ/mol which were 16 %, 13 %, and 18 % lower than those of without magnetic field at the same conditions with the highest CO_2 conversion, respectively. It was observed that the apparent activation energies with magnetic field These results evidently confirmed that the external magnetic field could promote the activity of *w*(Fe)-*w*(Cu)/MCM-41 catalysts in CO_2 hydrogenation as it enhanced the CO_2 conversion and concurrently decreased the energy consumption during the process.

As shown in Fig. 9, magnetic field not only enhanced CO_2 conversion but also led to high CH_3OH space time yield. The space-time yield of methanol ($mg_{methanol}/g_{catalyst}$ h) as a function of time-on-stream defined as follows:

$$\text{Space-time yield of methanol} = \frac{n_{\text{methanol}}}{[n_{CO_2}]_{\text{in}} \times m_{\text{catalyst}} \times V_{\text{m}}} \times v_{CO_2} \times MW_{\text{methanol}} \quad (4)$$

Where $n_{methanol}$ is moles methanol, n_{CO_2} is moles CO_2, $m_{catalyst}$ is total mass of catalyst, V_m is molar volume of ideal gas, 22 400 $cm^3\ mol^{-1}$, v_{CO_2} is volumetric flow rate of CO_2 ($cm^3\ min^{-1}$), and $MW_{methanol}$ is the molecular weight of methanol ($g\ mol^{-1}$). Without magnetic field, CH_3OH space time yields were 5.2 $mg/g_{catalyst}$ h, 4.8 $mg/g_{catalyst}$ h, and 42.7 $mg/g_{catalyst}$ h for 10(Cu)/MCM-41, 10(Fe)/MCM-41, and 10(Fe)-10(Cu)/MCM-41 catalysts, respectively. With

magnetic field, CH_3OH space time yields were 1.3 times, 1.7 times, and 1.5 times higher than those of without magnetic field for 10(Cu)/MCM-41, 10(Fe)/MCM-41, and 10(Fe)-10(Cu)/MCM-41 catalysts, respectively. For 10(Fe)-10(Cu)/MCM-41 catalyst, the highest CH_3OH space time yield (63.8 mg/$g_{catalyst}$ h) was obtained with magnetic flux density of –27.7 mT in N–S direction at 240 ^oC. It should be noted that the incorporation of Fe with Cu could significantly increase CH_3OH space time yield along with the increase of CO_2 conversion. Above 240 ^oC, CH_3OH space time yield decreased due to selective production of CO via reversed water-gas shift (RWGS) reaction (Taghdisian et al., 2015; Riaz et al., 2013). As a result, the performance of *w*(Fe)-*w*(Cu)/MCM-41 catalysts was improved when the external magnetic field was applied. This might be due to the enhancement of active metals with intrinsic magnetic property and CO_2 adsorption ability on magnetized metal surfaces.

Comparing the product distributions based on CO_2 conversion with magnetic field (Fig. 10B) at the condition which gave highest CO_2 conversion and without magnetic field (Fig. 10A), in both cases CO, CH_4, and CH_3OH were the main products. With magnetic field, CH_3OH yield was significantly increased, especially over 10(Fe)-10(Cu)/MCM-41 catalyst. In addition, 10(Cu)/MCM-41 catalyst led to higher CH_3OH and CO production, while 10(Fe)/MCM-41 catalyst was selective for CH_4 production. It was therefore concluded that the application of magnetic field in a packed bed reactor for CO_2 hydrogenation led to the advantages in a heterogeneously catalyzed reaction as it promoted methanol production, lowered the energy consumption, and reduced CO_2 emission, compared to the conventional reactor.

3.4. Energy conservation by the application of external magnetic field

The energy conservation is an important factor to take into account from the economic, environmental and industrial point of view. Concerning the catalyst performance and the energy consumption during the reaction over *w*(Fe)-*w*(Cu)/MCM-41 catalysts, relative

operating temperature under the magnetic field application calculated from the correlation between reaction temperatures and rates of reaction, and temperature saving expressed in the term of temperature difference between reaction temperature and relative operating temperature are listed in Table 4. The relative operating temperature under the magnetic field conditions which gave the highest CO_2 conversion (+20.8 mT in S–N direction for 10(Cu)/MCM-41 catalyst, and
–27.7 mT in N–S direction for both 10(Fe)/MCM-41 and 10(Fe)-10(Cu)/MCM-41 catalysts) were selected to compare with that of without magnetic field (the conventional reactor) at the same reaction rate. It was found that the relative operating temperatures of all catalysts with magnetic field were remarkably lower than that of without magnetic field. The temperature saving was in the range of 0.9–32.9 ^oC, 3.8–33.8 ^oC, and 18.6–57.7 ^oC for 10(Cu)/MCM-41, 10(Fe)/MCM-41 and 10(Fe)-10(Cu)/MCM-41 catalysts, respectively. With external magnetic field, the highest temperature saving was obtained at the reaction temperature of 260 ^oC which the operating temperatures were reduced by 1.14 times, 1.15 times, and 1.29 times compared to that one without magnetic field.

In addition, the environmental impact by means of the relative CO_2-eq mass emissions from CO_2 hydrogenation process in magnetic field-packed bed reactor was evaluated and compared to those of the conventional reactor. The calculation of CO_2 emission was based on hydrocarbon production process of 100 kg CO_2 conversion. As shown in Table 5, with magnetic field, CO_2 emission were significantly less than those without magnetic field at all reaction temperatures. CO_2 reduction by magnetic field were in the range of 46.4–187.8 kg, 28.8–314.7 kg, and 60.5–361.9 kg CO_2-eq for 10(Cu)/MCM-41, 10(Fe)/MCM-41, and 10(Fe)-10(Cu)/MCM-41 catalysts, respectively at the temperature range of 180–260 ^oC.

The preliminary economic evaluation was performed using 10(Fe)-10(Cu)/MCM-41 catalyst due to its outstanding temperature saving compared to other catalysts. The payback period was calculated from the costs of magnet and electric energy saving per year as shown

in Table 6. For the detail of calculation, the electric energy consumption was calculated from the total heat required to convert 100 kg of CO_2 in the time period of 1 h. The saving cost was then calculated from the difference between electric energy costs of the processes with and without magnetic field. The payback period for pilot plant scale was done based on the magnet price of 14.09 $/kg (June 2016: Alibaba group holding limited). It was found that electric energy costs at all reaction temperatures were significantly less than those without magnetic field. The saving costs by magnetic field were in the range of 2,074–48,373 $/a for 10(Fe)-10(Cu)/MCM-41 catalyst at the reaction temperature of 180–260 ºC. Accordingly, the payback periods were 4.7–0.2 a, respectively. As a result, this integrated magnetic field-packed bed reactor not only showed the outstanding performance in CO_2 consumption but also exhibited the excellent roles as it could lower the reaction temperature and CO_2 emission, resulting in the decrease of fuel consumption and operating cost, compared to that without magnetic field (the conventional reactor).

This effective CO_2 utilization would lead to a promising solution not only for energy issues due to the low thermal energy requirement for high methanol production but also for environmental pollution from CO_2 emission. Therefore, it can be concluded that the integrated magnetic field-packed bed reactor is of great potential application as it provides a green and sustainable innovation in chemical and petrochemical processes, and concurrently offers economic advantages in energy conservation by means of lowering the operating temperature.

Conclusion

In this work, the application of external magnetic field in a packed bed reactor is found to be a promising technique for improving the activity of *w*(Fe)-*w*(Cu)/MCM-41 catalysts with intrinsic magnetic property in CO_2 hydrogenation to methanol. With the

external magnetic field, CO_2 conversion and methanol production of all catalysts were significantly improved. The highest conversion and CH_3OH space time yield were obtained over 10(Fe)-10(Cu)/MCM-41 catalyst at magnetic flux density of –27.7 mT in N–S direction which were 1.8 times and 1.5 times higher than those without magnetic field; meanwhile, the lowest apparent activation energy (34.5 kJ/mol) was also achieved. Furthermore, with external magnetic field, the highest temperature saving was obtained at the reaction temperature of 260 ^oC which the operating temperatures were reduced by 0.9–32.9 ^oC, 3.8–33.8 ^oC, and 18.6–57.7 ^oC for 10(Cu)/MCM-41, 10(Fe)/MCM-41 and 10(Fe)-10(Cu)/MCM-41 catalysts, respectively compared to that without magnetic field. It was attributed to the fact that the application of magnetic field led to the advantages in a heterogeneously catalyzed reaction as it promoted CO_2 adsorption ability and methanol production. This process helps create opportunities to reduce CO_2 emission and energy consumption by lowering the operating temperature, and provides a green and sustainable innovation in chemical and petrochemical processes. The concept and potential use of this integrated magnetic field-packed bed reactor, here begun with CO_2 utilization, will be further expanded to other chemical production from greenhouse gases in our future work.

Acknowledgments

This work was financially supported by grants from the Thailand Research Fund (TRF) and Kasetsart University through the Royal Golden Jubilee Ph.D. Fellowship (Grant No. PHD/0283/2552), and the Kasetsart University Research and Development Institute (KURDI). The support from the Synchrotron Light Research Institute (SLRI) (Public Organization), Thailand for XAS analysis is acknowledged.

Symbols and abbreviations

2θ	Angle of diffraction
A	Ampere
a.u.	Arbitrary unit
B	Magnetic flux density
BET	Brunauer-Emmett-Teller
BJH	Barrett-Joyner-Halenda
CTAB	Cetyltrimethyl ammonium bromide
d	Pore size
d_{i}	Inside diameter
d_{o}	Outside diameter
E_{a}	Apparent activation energy
EDS	Energy-dispersive x-ray spectroscopy
FID	Flame ionization detection
FTS	Fischer-Tropsch synthesis
GC	Gas chromatograph
H_{c}	Coercivity field
HR-TEM	High-resolution transmission electron microscopy
k_{a}	Rate constant
LCF	Linear combination fitting
M	Magnetization
m/z	Mass-to-charge ratio
m_{catalyst}	Total mass of catalyst
MCM-41	Mobil Composition of Matter No. 41
M_{r}	Remanence magnetization
M_{s}	Saturation magnetization

$MW_{methanol}$	The molecular weight of methanol
$n_{methanol}$	Moles methanol
n_{CO2}	Moles CO_2
N–S	North-to-south
p/p_0	Relative pressure
R	Gas constant
RWGS	Reverse water-gas shift
s	Space velocity
S–N	South-to-north
STEM	Scanning transmission electron microscopy
t	Reaction temperature (^oC)
T	Reaction temperature (K)
T	Tesla
TCD	Thermal conductivity detector
TEOS	Tetraethyl orthosilicate
TPD	Temperature-programmed desorption
TPR	Temperature-programmed reduction
TRXAS	Time-resolved x-ray absorption spectroscopy
v	Specific volume of gas adsorbed
v_{CO2}	Volumetric flow rate of CO_2
v_{total}	The volumetric flow rate of total reactant gases
V_m	Molar volume of ideal gas
V_R	Reactor volume
VSM	Vibrating sample magnetometer
w	Mass fraction
XANES	X-ray absorption near edge structure

X_{CO2} Fractional conversion of CO_2

XRD X-ray diffraction

References

Ajaikumar, S., Pandurangan, A., 2009. Efficient synthesis of quinoxaline derivatives over ZrO2/M_xO_y (M = Al, Ga, In and La) mixed metal oxides supported on MCM-41 mesoporous molecular sieves. Applied Catalysis A: General 357, 184–192.

Alothman, Z. A., 2012. A Review: Fundamental Aspects of Silicate Mesoporous Materials. Materials 5, 2874–2902.

Angelo, L., Kobl, K., Tejada, L. M. M., Zimmermann, Y., Parkhomenko, K., Roger, A. C., 2015. Study of $CuZnMO_x$ oxides (M = Al, Zr, Ce, CeZr) for the catalytic hydrogenation of CO_2 into methanol. Comptes Rendus Chimie 18, 250–260.

Arena, F., Mezzatesta, G., Zafarana, G., Trunfio, G., Frusteri, F., Spadaro, L., 2013. Effects of oxide carriers on surface functionality and process performance of the Cu-ZnO system in the synthesis of methanol via CO_2 hydrogenation. Journal of Catalysis 300, 141–151.

Bao, Z., Ding, W., Li, Q., 2012. Effect of Fe/Cu ratio on the activity of Fe-Al-Cu catalysts for water gas shift reaction under hydrogen-rich atmosphere. International Journal of Hydrogen Energy 37, 951–955.

Bonura, G., Cordaro, M., Cannilla, C., Frusteri, F., 2014. The changing nature of the active site of Cu-Zn-Zr catalysts for the CO_2 hydrogenation reaction to methanol. Applied Catalysis B: Environmental 152–153, 152–161.

Chinniyomphanich, U., Wongwanichsin, P., Jitkarnka, S., 2016. Sn_xO_y/SAPO-34 as catalysts for catalytic dehydration of bio-ethanol: impacts of oxidation state, interaction, and loading amount. Journal of Cleaner Production 111, 25–33.

Fernandez, J. R. Abanades, J.C., 2016. CO_2 capture from the calcination of $CaCO_3$ using iron oxide as heat carrier. Journal of Cleaner Production 112, 1211–1217.

Huisingh, D., Zhang, Z., Moore, J. C., Qiao, Q., Li, Q., 2015. Recent advances in carbon emissions reduction: policies, technologies, monitoring, assessment and modeling. Journal of Cleaner Production 103, 1–12.

Hyde, T. I., 2008. Final Analysis: Crystallite Size Analysis of Supported Platinum Catalysts by XRD. Platinum Metals Review 52, 129–130.

Jiang, X., Koizumi, N., Guo, X., Song, C., 2015. Bimetallic Pd-Cu catalysts for selective CO_2 hydrogenation to methanol. Applied Catalysis B: Environmental 170–171, 173–185.

Kiatphuengporn, S., Chareonpanich, M., Limtrakul, J., 2014. Effect of unimodal and bimodal MCM-41 mesoporous silica supports on activity of Fe-Cu catalysts for CO_2 hydrogenation. Chemical Engineering Journal 240, 527–533.

Li, B., Wu, K., Yuan, T., Han, C., Xu, J., Pang, X., 2012. Synthesis, characterization and catalytic performance of high iron content mesoporous Fe-MCM-41. Microporous and Mesoporous Materials 151, 277–281.

Luu, M.T., Milani, D., Abbas, A., 2016. Analysis of CO_2 utilization for methanol synthesis integrated with enhanced gas recovery. Journal of Cleaner Production 112, 3540–3554.

Mohsenzadeh, A., Richards, T., Bolton, K., 2016. DFT study of the water gas shift reaction on Ni(111), Ni(100) and Ni(110) surfaces. Surface Science 644, 53–63.

Okumura, H., Endo, S., Joonwichien, S., Yamasue, E., Ishihara, K. N., 2015. Magnetic field effect on heterogeneous photocatalysis. Catalysis Today 258, 634–647.

Onodera, R., Kimura, S., Watanabe, K., Yokoyama, Y., Makino, A., Koyama, K., 2014. Crystallization kinetics of high iron concentration amorphous alloys under high magnetic field. Journal of Alloys and Compounds 604, 8–11.

Phukan, A. C., Boruah, R. K., 1999. Extraction and evaluation of microcrystalline wax from press mud waste of the sugar industry. Separation and Purification Technology 17, 189–194.

Radhakrishnan, B., Nicholson, D. M., Eisenbach, M., Parish, C., Ludtka, G. M., Rios, O., 2015. Alignment of iron nanoparticles in a magnetic field due to shape anisotropy. Journal of Magnetism and Magnetic Materials 394, 481–490.

Rafati, M., Wang, L., Shahbazi, A., 2015. Effect of silica and alumina promoters on co-precipitated Fe-Cu-K based catalysts for the enhancement of CO_2 utilization during Fischer-Tropsch synthesis. Journal of CO_2 Utilization 12, 34–42.

Ren, H., Xu, C. H., Zhao, H. Y., Wang, Y. X., Liu, J., Liu, J. Y., 2015. Methanol synthesis from CO_2 hydrogenation over Cu/g-Al_2O_3 catalysts modified by ZnO, ZrO_2 and MgO. Journal of Industrial and Engineering Chemistry 28, 261–267.

Riaz, A., Zahedi, G., Klemeš, J. J., 2013. A review of cleaner production methods for the manufacture of methanol. Journal of Cleaner Production 57, 19–37.

Romero-Sáez, M., Divakar, D., Aranzabal, A., González-Velasco, J. R., González-Marcos, J. A., 2016. Catalytic oxidation of trichloroethylene over Fe-ZSM-5: Influence of the preparation method on the iron species and the catalytic behavior. Applied Catalysis B: Environmental 180, 210–218.

Suo, H., Zhang, C., Wu, B., Xu, J., Yang, Y., Xiang, H., Li, Y., 2012. A comparative study of Fe/SiO_2 Fischer-Tropsch synthesis catalysts using tetraethoxysilane and acidic silica sol as silica sources. Catalysis Today 183, 88–95.

Tu, R., Jin, W., Xi, T., Yang, Q., Han, S. F., Abomohra, A. E., 2015. Effect of static magnetic field on the oxygen production of Scenedesmus obliquus cultivated in municipal wastewater. Water Research 86, 132–138.

Taghdisian, H., Pishvaie, M. R., Farhadi, F., 2015. Multi-objective optimization approach for green design of methanol plant based on CO_2-efficeincy indicator. Journal of Cleaner Production 103, 640–650.

Torshizi, H. O., Mirzaei, A. A., Bayat, M. H., Sarani, R., Azizi, H. R., Vahid, S., Golzarpour, H. R., 2015. Kinetics studies of fused Fe-Co-Mn (ternary) catalyst in Fischer-Tropsch synthesis. Journal of Environmental Chemical Engineering 3, 2243–2252.

Udagawa, C., Fukuyoshi, S., Morimoto, S., Tanimoto, Y., Nakagaki, R., 2011. Photochemistry of flutamide in various media: Investigation of the reaction mechanism as revealed by external magnetic field effects on product yields. Journal of Photochemistry and Photobiology A: Chemistry 226, 57–63.

Van-Dal, É. S., Bouallou, C., 2013. Design and simulation of a methanol production plant from CO_2 hydrogenation. Journal of Cleaner Production 57, 38–45.

Wang, J., Sugawara-Narutaki, A., Shimojima, A., Okubo, T., 2012. Biphasic synthesis of colloidal mesoporous silica nanoparticles using primary amine catalysts. Journal of Colloid and Interface Science 385, 41–47.

Wang, Y., Zhang, Q., Shishido, T., Takehira, K., 2002. Characterizations of iron-containing MCM-41 and its catalytic properties in epoxidation of styrene with hydrogen peroxide. Journal of Catalysis 209**,** 186–196.

Yang, N., Wang, R., 2015. Sustainable technologies for the reclamation of greenhouse gas CO_2. Journal of Cleaner Production 103, 784–792.

Zhan, H., Li, F., Gao, P., Zhao, N., Xiao, F., Wei, W., Zhong, L., Sun, Y., 2014. Methanol synthesis from CO_2 hydrogenation over $La_eM_eCu_eZn_eO$ (M = Y, Ce, Mg, Zr) catalysts derived from perovskite-type precursors. Journal of Power Sources 251, 113–121.

Zhang, H., Chu, W., Xu, H., Zhou, J., 2010. Plasma-assisted preparation of Fe-Cu bimetal catalyst for higher alcohols synthesis from carbon monoxide hydrogenation. Fuel 89, 3127–3131.

Zhang, Q., Wang, Y., Ohishi, Y., Shishido, T., Takehira, K., 2001. Vanadium-Containing MCM-41 for Partial Oxidation of Lower Alkanes. Journal of Catalysis 202, 308–318.

Zhang, Z., Moore, J. C., Huisingh, D., Zhao, Y., 2015. Review of geoengineering approaches to mitigating climate change. Journal of Cleaner Production 103, 898–907.

Zheng, X., Wang, Y., Lu, D., 2015. A realistic description of influence of the magnetic field strength on high gradient magnetic separation. Minerals Engineering 79, 94–101.

Zhou, Y., Wang, S., Xiao, M., Han, D., Lu, Y., Meng, Y., 2015. Formation of dimethyl carbonate on natural clay supported bimetallic Cu-Ni catalysts. Journal of Cleaner Production 103, 925–933.

Zou, Q. C., Jie, J. C., Liu, S. C., Wang, T. M., Yin, G. M., Li, T. J., 2015. Effect of traveling magnetic field on separation and purification of Si from Al-Si melt during solidification. Journal of Crystal Growth 429, 68–73.

Figure Captions

Figure 1 Schematic diagram of a magnetic field-assisted, continuous-flow packed bed reactor system and gradient of magnetic flux density of a) two pairs and b) four pairs of Alnico magnets positioned over the reactor.

■ –(20–30) mT ■ –(10–20) mT ■ –(0–10) mT ■ +(0–10) mT ■ +(10–20) mT

Figure 2 (A) Nitrogen adsorption-desorption isotherms and (B) pore size distribution of (a) MCM-41 support, (b) 10(Cu)/MCM-41, (c) 10(Fe)/MCM-41, and (d) 10(Fe)-10(Cu)/MCM-41 catalysts.

Figure 3 XRD patterns of (a) calcined 10(Cu)/MCM-41, (b) reduced 10(Cu)/MCM-41, (c) calcined 10(Fe)/MCM-41, (d) reduced 10(Fe)/MCM-41, (e) calcined 10(Fe)-10(Cu)/MCM-41, and (f) reduced 10(Fe)-10(Cu)/MCM-41 catalysts.

▲ CuO △ Cu^0 ● Fe_2O_3 ○ Fe^0

Figure 4 TEM images of (a) 10(Cu)/MCM-41, (b) 10(Fe)/MCM-41, (c) 10(Fe)-10(Cu)/MCM-41 catalysts, (d) CuO particle dispersion, and (e) Fe_2O_3 particle dispersion.

Figure 5 H_2-TPR profiles of (a) 10(Cu)/MCM-41, (b) 10(Fe)/MCM-41, and (c) 10(Fe)-10(Cu)/MCM-41 catalysts.

TPR profile (experiment) TPR profile (program)

Deconvoluted profile of Fe and Cu oxide species

Figure 6 Normalized Fe K-edge XANES spectra of (a) 10(Fe)/MCM-41, and (b) 10(Fe)-10(Cu)/MCM-41 catalysts measured during reduction in hydrogen at room temperature to 480 ^oC and holding for 3 h.

Figure 7 Magnetic hysteresis loops of (a) before and (b) after reduction process at 480 ^oC.

10(Cu)/MCM-41 10(Fe)/MCM-41 10(Fe)–10(Cu)/MCM-41

Figure 8 CO_2-TPD profiles of reduced (a) MCM-41 support, (b) 10(Cu)/MCM-41, (c) 10(Fe)/MCM-41, and (d) 10(Fe)-10(Cu)/MCM-41 catalysts.

CO_2-TPD profile (experiment) CO_2-TPD profile (program)

Deconvoluted profile of CO_2 desorption

Figure 9 The catalytic performance in term of CO_2 conversion and CH_3OH space time yield as a function of the reaction temperature at different magnetic field direction and flux density over (a) 10(Cu)/MCM-41, (b) 10(Fe)/MCM-41, and (c) 10(Fe)-10(Cu)/MCM-41 catalysts.

0 mT +20.8 mT, S–N +27.7 mT, S–N

–20.8 mT, N–S –27.7 mT, N–S

Figure 10 Product distribution (A) without magnetic field and (B) with magnetic field over (a) 10(Cu)/MCM-41 (0 mT), (b) 10(Cu)/MCM-41 (+20.8 mT, S–N), (c) 10(Fe)/MCM-41 (0 mT), (d) 10(Fe)/MCM-41 (–27.7 mT, N–S), (e) 10(Fe)-10(Cu)/MCM-41 (0 mT), and (f) 10(Fe)-10(Cu)/MCM-41 (–27.7 mT, N–S).

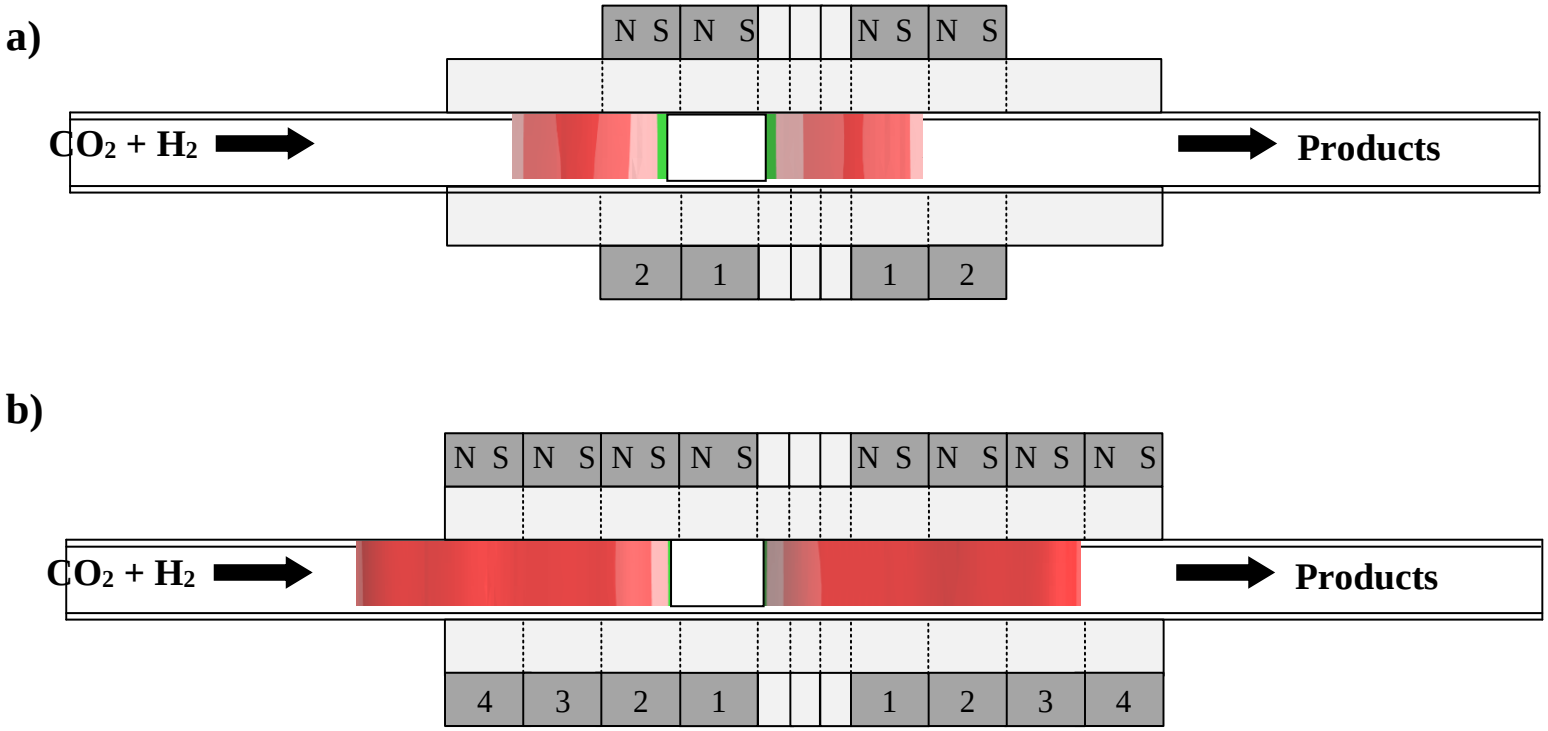

Title of the manuscript: Cleaner production of methanol from carbon dioxide over copper and iron supported MCM-41 catalysts using innovative integrated magnetic field-packed bed reactor

Authors: Sirapassorn Kiatphuengporn, Waleeporn Donphai, Pongsakorn Jantaratana, Nevzat Yigit, Karin Föttinger, Günther Rupprechter, Metta Chareonpanich

Figure number: 1

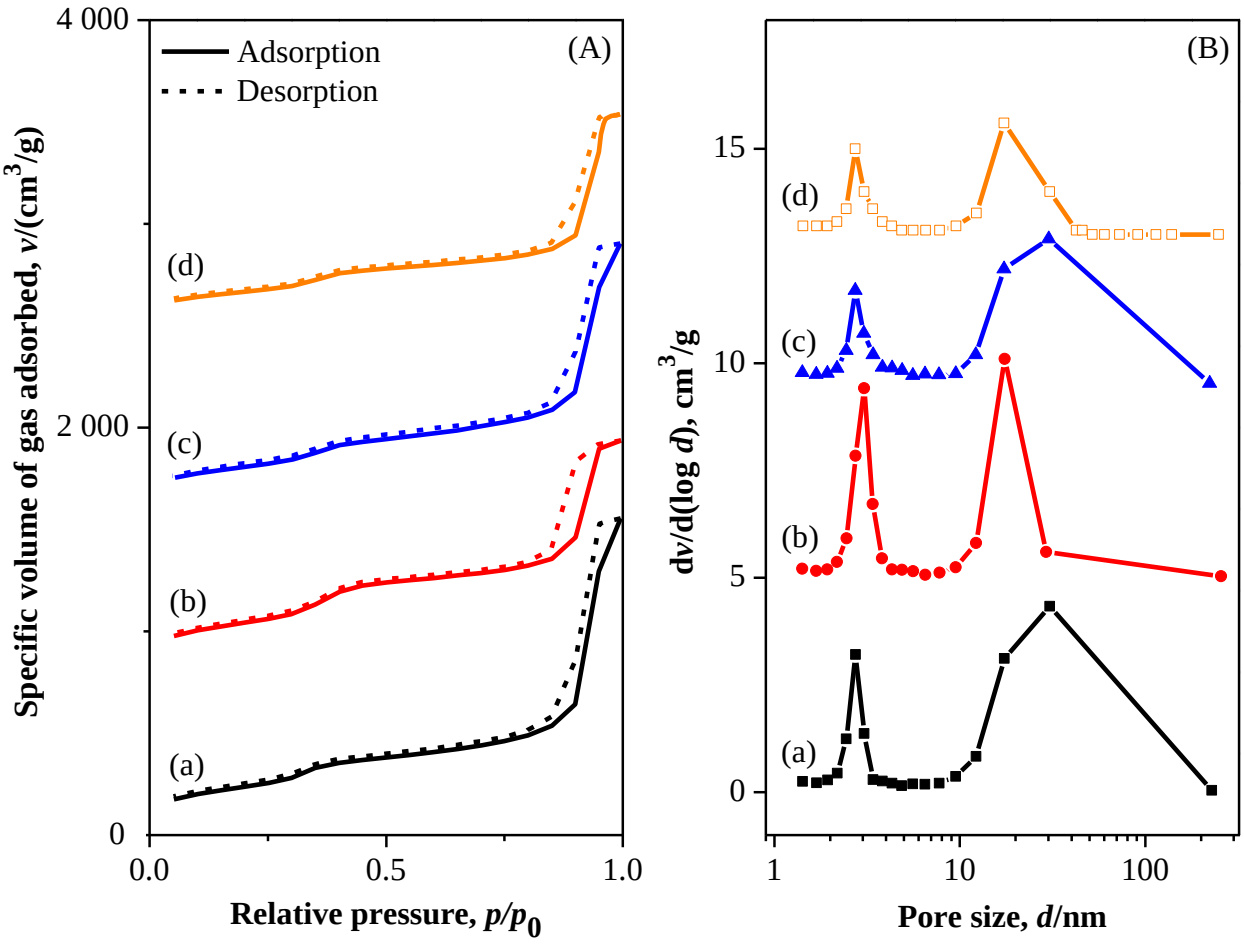

Title of the manuscript: Cleaner production of methanol from carbon dioxide over copper and iron supported MCM-41 catalysts using innovative integrated magnetic field-packed bed reactor

Authors: Sirapassorn Kiatphuengporn, Waleeporn Donphai, Pongsakorn Jantaratana, Nevzat Yigit, Karin Föttinger, Günther Rupprechter, Metta Chareonpanich

Figure number: 2

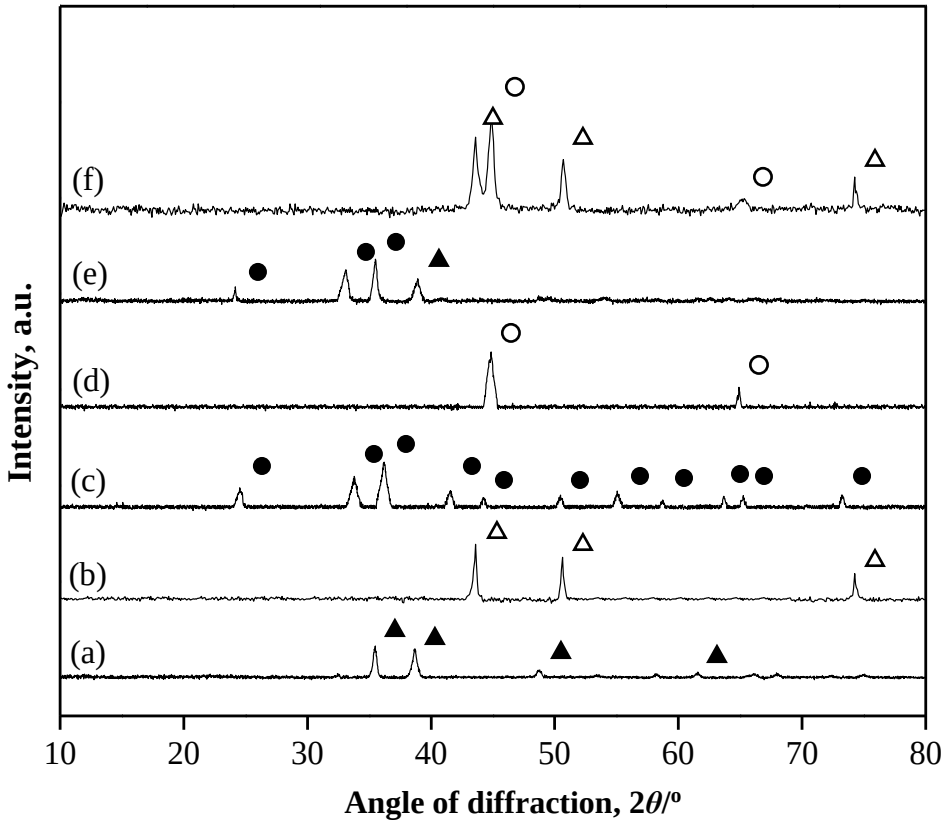

Title of the manuscript: Cleaner production of methanol from carbon dioxide over copper and iron supported MCM-41 catalysts using innovative integrated magnetic field-packed bed reactor

Authors: Sirapassorn Kiatphuengporn, Waleeporn Donphai, Pongsakorn Jantaratana, Nevzat Yigit, Karin Föttinger, Günther Rupprechter, Metta Chareonpanich

Figure number: 3

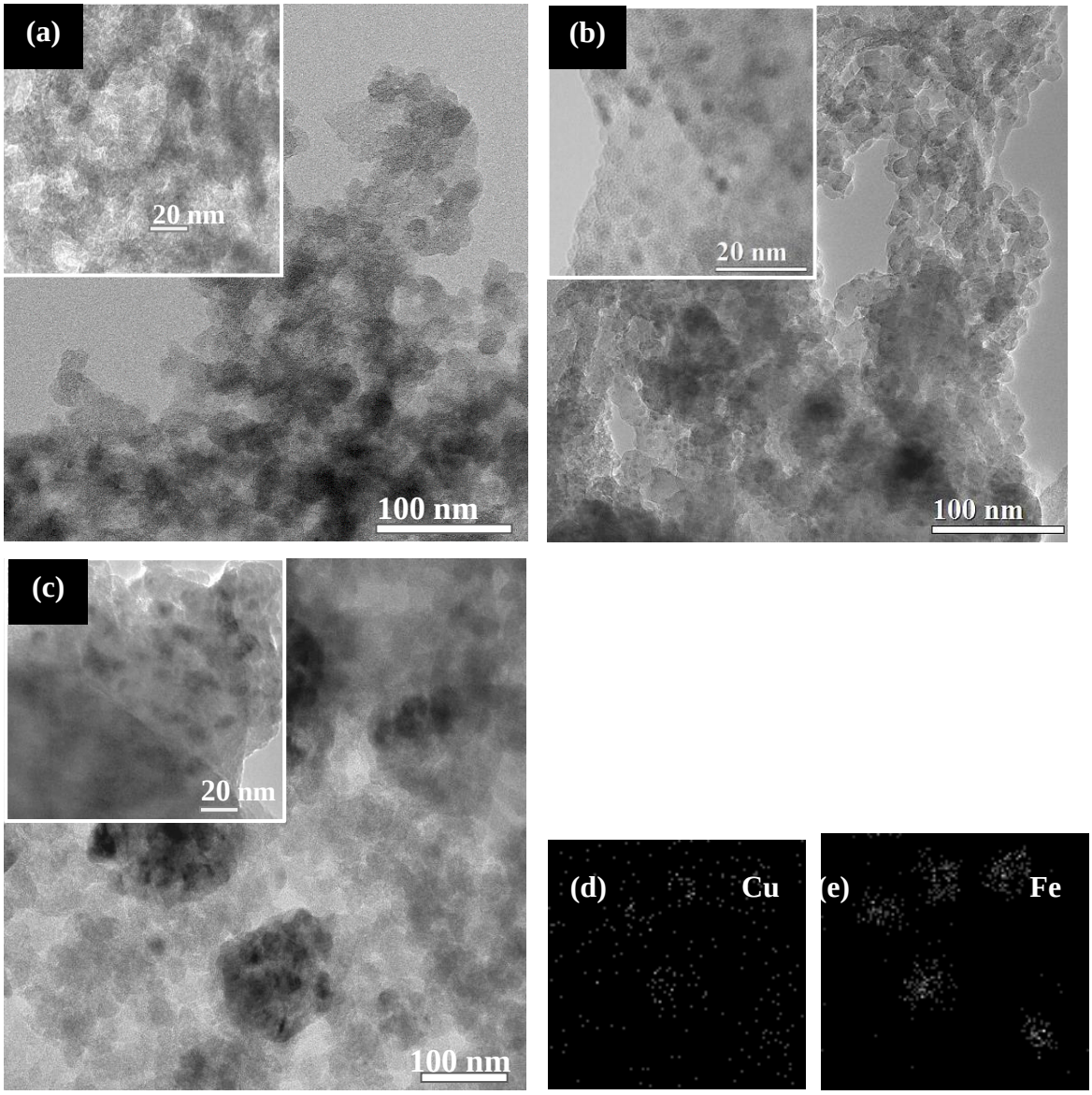

Title of the manuscript: Cleaner production of methanol from carbon dioxide over copper and iron supported MCM-41 catalysts using innovative integrated magnetic field-packed bed reactor

Authors: Sirapassorn Kiatphuengporn, Waleeporn Donphai, Pongsakorn Jantaratana, Nevzat Yigit, Karin Föttinger, Günther Rupprechter, Metta Chareonpanich

Figure number: 4

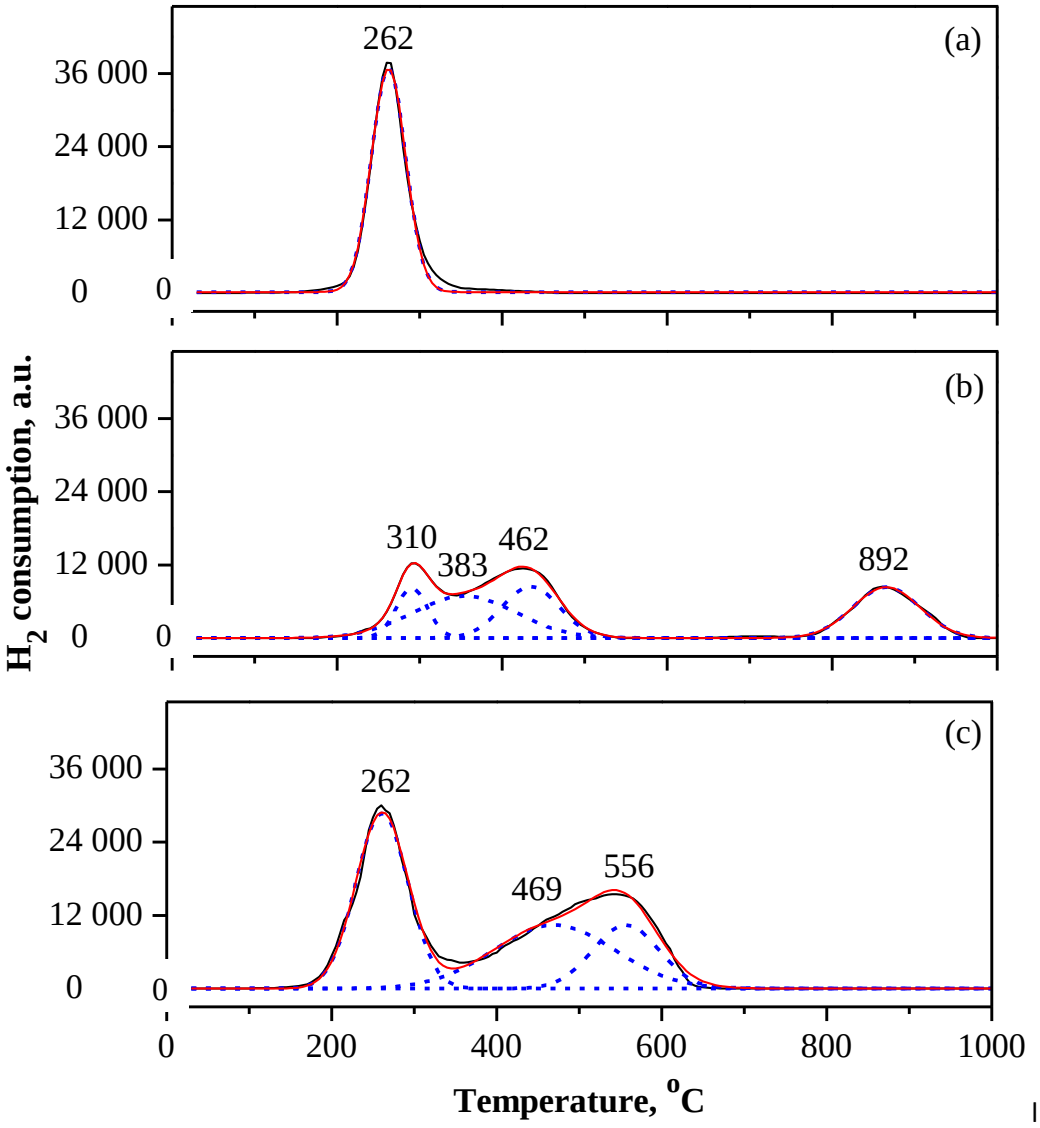

Title of the manuscript: Cleaner production of methanol from carbon dioxide over copper and iron supported MCM-41 catalysts using innovative integrated magnetic field-packed bed reactor

Authors: Sirapassorn Kiatphuengporn, Waleeporn Donphai, Pongsakorn Jantaratana, Nevzat Yigit, Karin Föttinger, Günther Rupprechter, Metta Chareonpanich

Figure number: 5

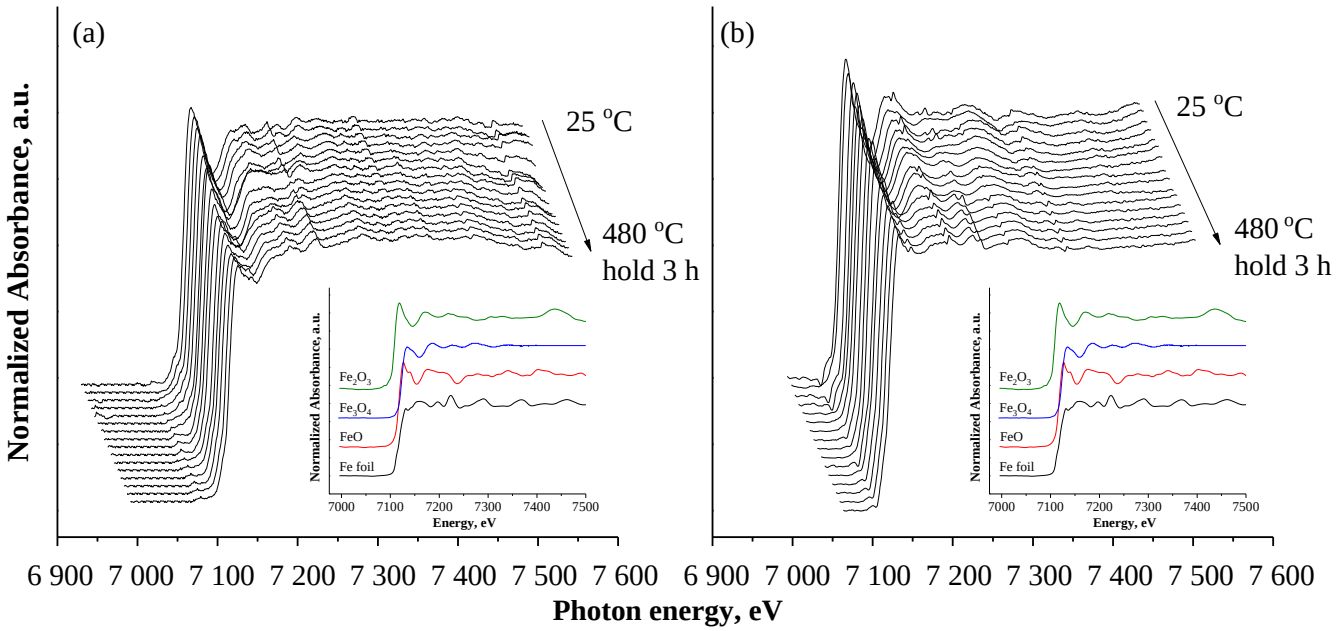

Title of the manuscript:	Cleaner production of methanol from carbon dioxide over copper and iron supported MCM-41 catalysts using innovative integrated magnetic field-packed bed reactor
Authors:	Sirapassorn Kiatphuengporn, Waleeporn Donphai, Pongsakorn Jantaratana, Nevzat Yigit, Karin Föttinger, Günther Rupprechter, Metta Chareonpanich
Figure number:	6

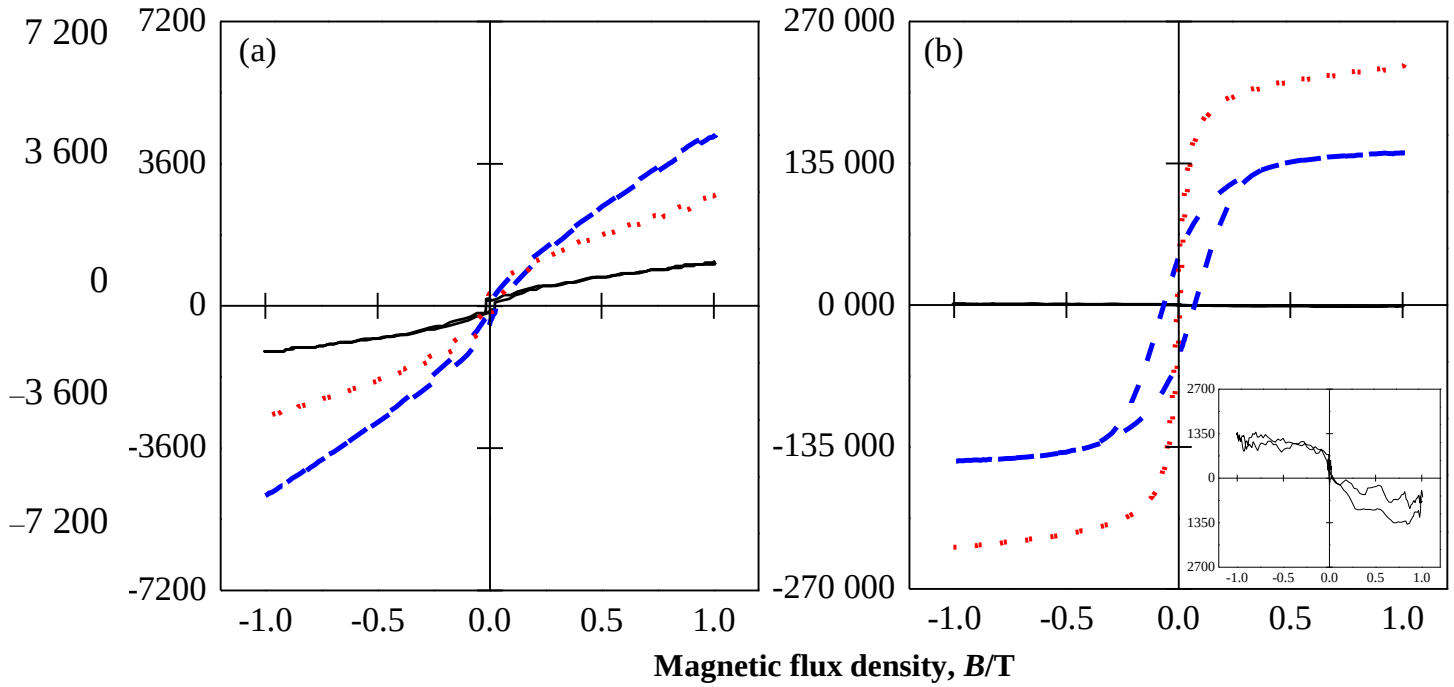

Title of the manuscript: Cleaner production of methanol from carbon dioxide over copper and iron supported MCM-41 catalysts using innovative integrated magnetic field-packed bed reactor

Authors: Sirapassorn Kiatphuengporn, Waleeporn Donphai, Pongsakorn Jantaratana, Nevzat Yigit, Karin Föttinger, Günther Rupprechter, Metta Chareonpanich

Figure number: 7

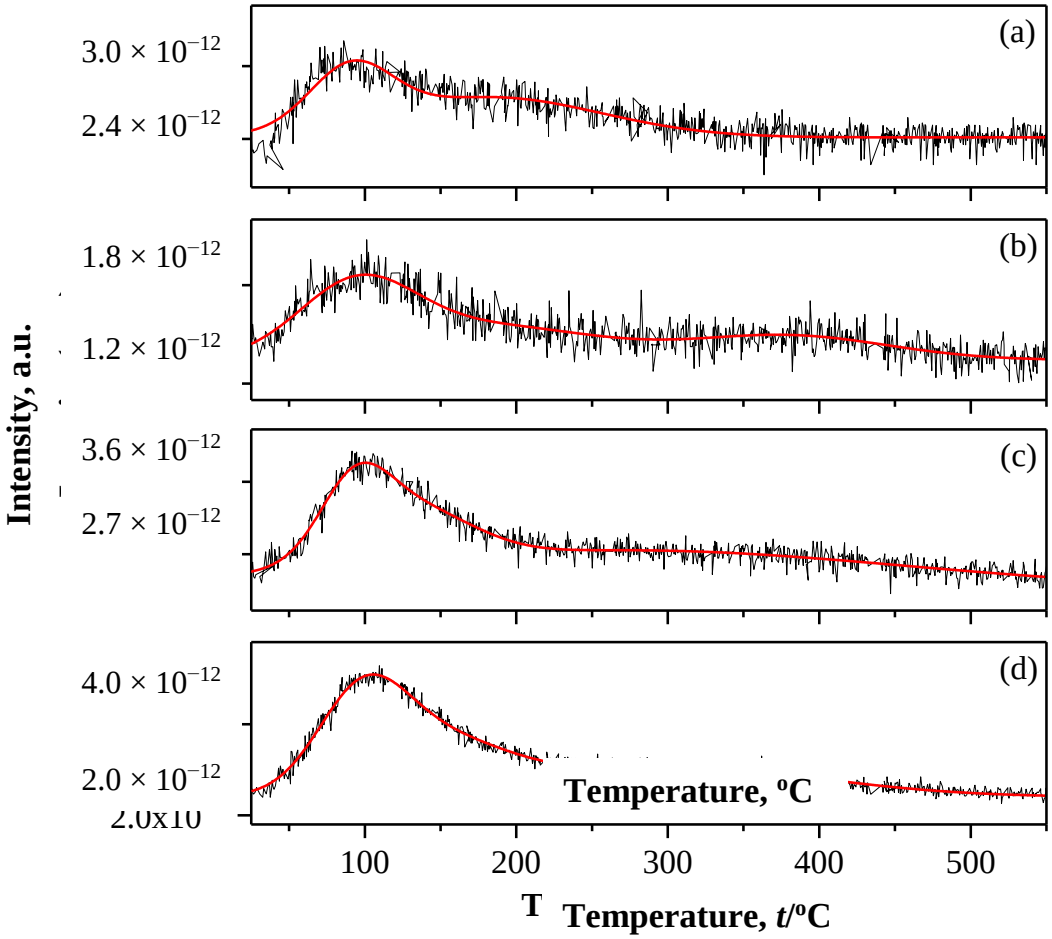

Title of the manuscript: Cleaner production of methanol from carbon dioxide over copper and iron supported MCM-41 catalysts using innovative integrated magnetic field-packed bed reactor

Authors: Sirapassorn Kiatphuengporn, Waleeporn Donphai, Pongsakorn Jantaratana, Nevzat Yigit, Karin Föttinger, Günther Rupprechter, Metta Chareonpanich

Figure number: 8

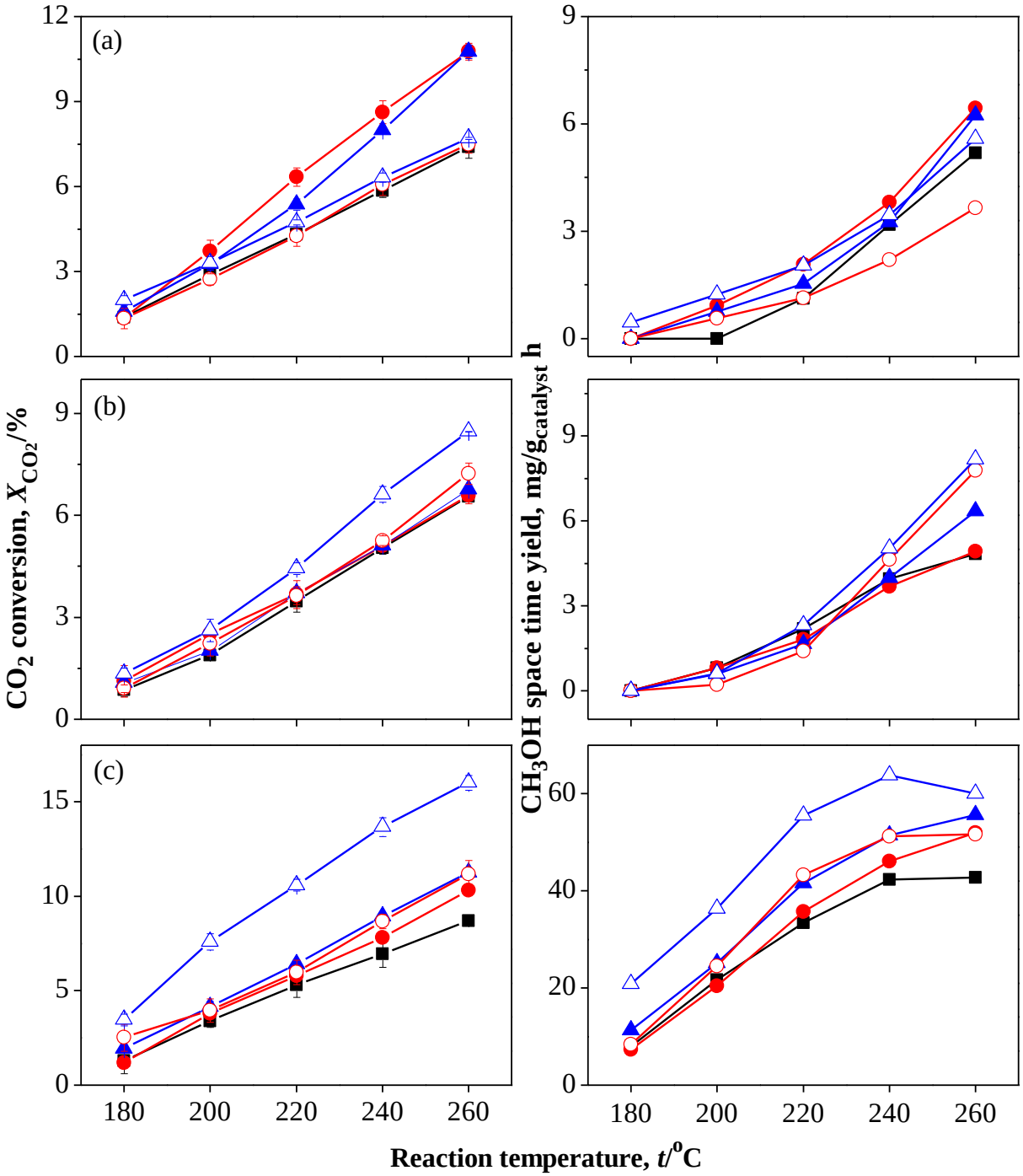

Title of the manuscript: Cleaner production of methanol from carbon dioxide over copper and iron supported MCM-41 catalysts using innovative integrated magnetic field-packed bed reactor

Authors: Sirapassorn Kiatphuengporn, Waleeporn Donphai, Pongsakorn Jantaratana, Nevzat Yigit, Karin Föttinger, Günther Rupprechter, Metta Chareonpanich

Figure number: 9

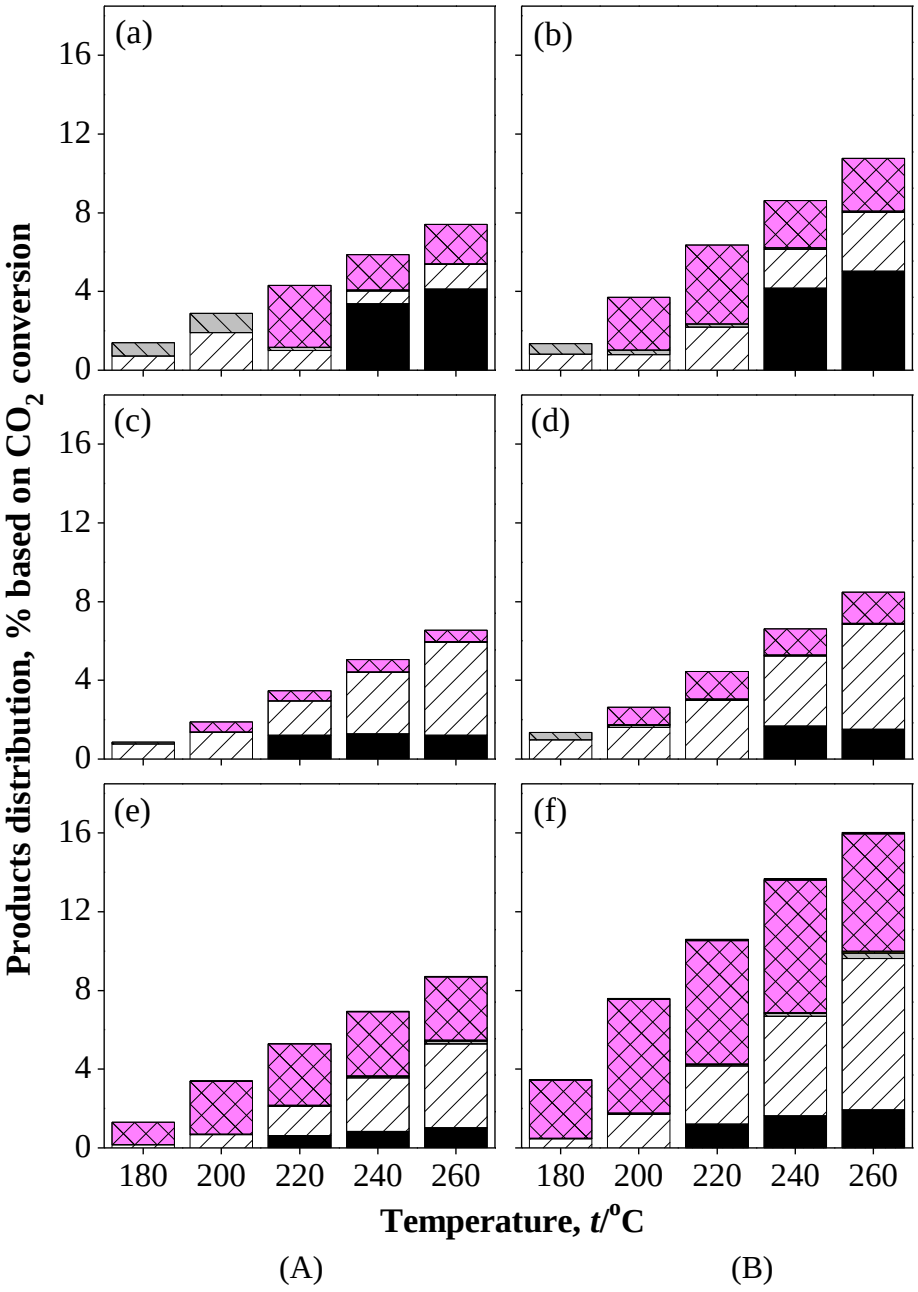

Title of the manuscript: Cleaner production of methanol from carbon dioxide over copper and iron supported MCM-41 catalysts using innovative integrated magnetic field-packed bed reactor

Authors: Sirapassorn Kiatphuengporn, Waleeporn Donphai, Pongsakorn Jantaratana, Nevzat Yigit, Karin Föttinger, Günther Rupprechter, Metta Chareonpanich

Figure number: 10

Table 1

Specific surface area, specific pore volume, average pore size and relative CO_2 adsorption capacity of MCM-41 support and *w*(Fe)-*w*(Cu)/MCM-41 catalysts, and crystallite size of CuO and Fe_2O_3.

Catalysts	Specific surface area, m^2/g	Specific pore volume, m^3/g	Pore size, nm	Crystallite size[a], nm		Relative CO_2 adsorption capacity[b]
				CuO	Fe_2O_3	
MCM-41	870	2.4	2.7 , 30.5	-	-	1.00
10(Cu)/MCM-41	888	1.8	2.7, 17.5	20.4 (24.3)	-	1.09
10(Fe)/MCM-41	756	2.0	2.7 , 30.1	-	16.7 (3.9)	3.57
10(Fe)-10(Cu)/MCM-41	605	1.6	2.7, 17.2	19.6	31.3	4.91

[a] Calculated from the Scherrer equation and measured from TEM image (in parentheses)
[b] Calculated by using the area under the CO_2-TPD profiles and compared to that of MCM-41

Table 2

Results from linear combination fitting (LCF) analysis of *w*(Fe)-*w*(Cu)/MCM-41 catalysts before and after reduction process at 480 ^oC.

Catalysts	Mass fraction, *w*/%			
	Fe_2O_3	Fe_3O_4	FeO	Fe foil
10(Fe)/MCM-41	73.0	24.7	2.3	-
Reduced 10(Fe)/MCM-41	11.3	3.8	44.2	40.7
10(Fe)-10(Cu)/MCM-41	81.6	14.7	3.7	-
Reduced 10(Fe)-10(Cu)/MCM-41	16.3	6.4	31.7	45.6

Table 3

Apparent activation energy of *w*(Fe)-*w*(Cu)/MCM-41 catalysts in CO_2 hydrogenation reaction.

Magnetic flux density at the center of catalyst bed, mT	Apparent activation energy, E_a/(kJ/mol)					
	10(Cu)/MCM-41		10(Fe)/MCM-41		10(Fe)-10(Cu)/MCM-41	
	S–N	N–S	S–N	N–S	S–N	N–S
0.0	44.8	44.8	47.7	47.7	42.0	42.0
±20.8	37.6	44.0	47.0	45.5	40.5	40.0
±27.7	38.6	42.8	46.6	41.6	39.4	34.5

Table 4

Relative operating temperature and temperature saving of *w*(Fe)-*w*(Cu)/MCM-41 catalysts under the magnetic field application in CO_2 hydrogenation reaction.

Reaction temperature, *t*/°C	10(Cu)/MCM-41		10(Fe)/MCM-41		10(Fe)-10(Cu)/MCM-41	
	Relative temperature[a], °C	Temperature saving, °C	Relative temperature[b], °C	Temperature saving, °C	Relative temperature[c], °C	Temperature saving, °C
180	179.1	0.9	176.2	3.8	161.4	18.6
200	191.1	8.9	185.2	14.8	172.9	27.1
220	202.4	17.6	199.2	20.8	183.8	36.2
240	214.8	25.2	213.0	27.0	192.5	47.5
260	227.1	32.9	226.2	33.8	202.3	57.7

[a] Calculated by using the equation: $R = 4.8 \times 10^{-11} t - 8.1 \times 10^{-9}$

[b] Calculated by using the equation: $R = 4.2 \times 10^{-11} t - 7.0 \times 10^{-9}$

[c] Calculated by using the equation: $R = 5.9 \times 10^{-11} t - 9.1 \times 10^{-9}$ where R is the rate of reaction (mol/min) and t is reaction temperature (°C)

Table 5

Total CO_2-eq emissions from CO_2 hydrogenation process, based on 100 kg CO_2 conversion with and without the magnetic field application over *w*(Fe)-*w*(Cu)/MCM-41 catalysts.

Reaction temperature, *t*/°C	10(Cu)/MCM-41			10(Fe)/MCM-41			10(Fe)-10(Cu)/MCM-41		
	Total CO_2-eq emissions, kg		CO_2-eq reduction by magnetic field[c], kg	Total CO_2-eq emissions, kg		CO_2-eq reduction by magnetic field[c], kg	Total CO_2-eq emissions, kg		CO_2-eq reduction by magnetic field[c], kg
	Without magnetic field[a]	+20.8 mT, S–N[b]		Without magnetic field[a]	–27.7 mT, N–S[b]		Without magnetic field[a]	–27.7 mT, N–S[b]	
180	517.9	330.1	187.8	865.5	550.8	314.7	579.2	217.3	361.9
200	282.3	220.2	62.1	451.5	335.6	115.9	251.0	112.6	138.4
220	211.6	144.0	67.6	294.1	237.3	56.8	179.6	90.2	89.4
240	172.0	116.9	55.1	228.8	191.6	37.2	151.9	77.1	74.8
260	149.0	102.6	46.4	176.3	147.5	28.8	132.6	72.1	60.5

[a] CO_2 emission from process electricity calculated from the grid electricity emission factor (0.6093)

[b] CO_2 emission from electricity and magnetic material production (calculated from databases of Ecoinvent 2.2, IPPC 2007, GWP100a, and U.S. LCI)

[c] Calculated from the difference of CO_2 emissions from CO_2 hydrogenation processes with and without magnetic field

Table 6

Electric energy saving costs and payback periods of the process with and without magnetic field over 10(Fe)-10(Cu)/MCM-41catalyst

Reaction temperature, *t*/°C	10(Fe)-10(Cu)/MCM-41			
	Electric energy cost[a], $/a		Saving cost[b], $/a	Payback period[c], a
	Without magnetic field	–27.7 mT, N–S		
180	16,725	14,651	2,074	4.7
200	54,863	46,117	8,746	1.1
220	95,973	77,688	18,285	0.5
240	139,879	108,240	31,639	0.3
260	192,823	144,450	48,373	0.2

[a]Calculated based on the average electricity cost from Thailand Board of Investment (June 2016: 0.1 $/kWh)

[b]Calculated from the difference of electric energy cost from CO_2 hydrogenation processes with and without magnetic field

[c]Calculated based on the Alnico magnet price of 14.09 $/kg (June 2016: Alibaba group holding limited), and the reactor diameter of 0.66 m with the catalyst bed length of 1.66 m

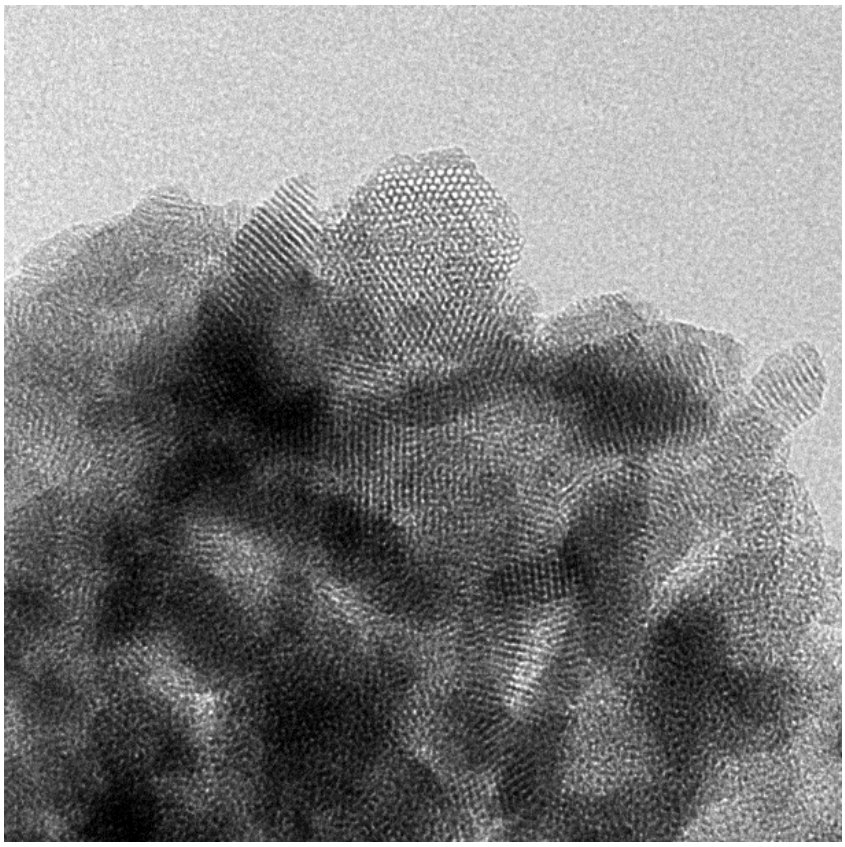

Figure 1 (Supplementary information)

The structure of MCM-41 mesoporous silica.

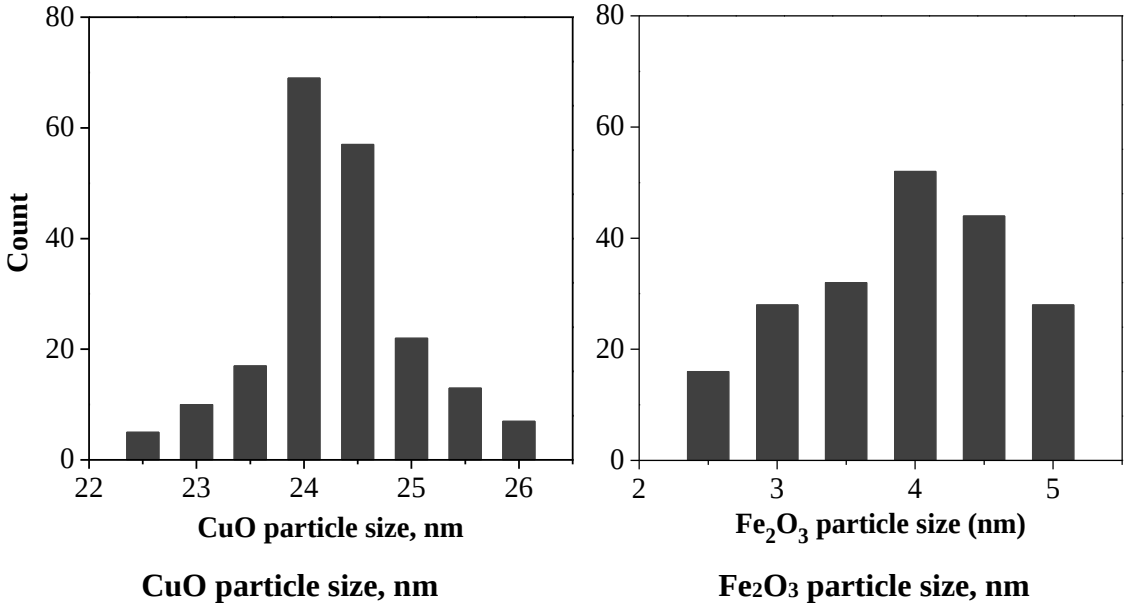

CuO particle size, nm **Fe2O3 particle size, nm**

Figure 2 (Supplementary information)

Histograms of particle size distribution of (a) 10(Cu)/MCM-41, (b) 10(Fe)/MCM-41 catalysts

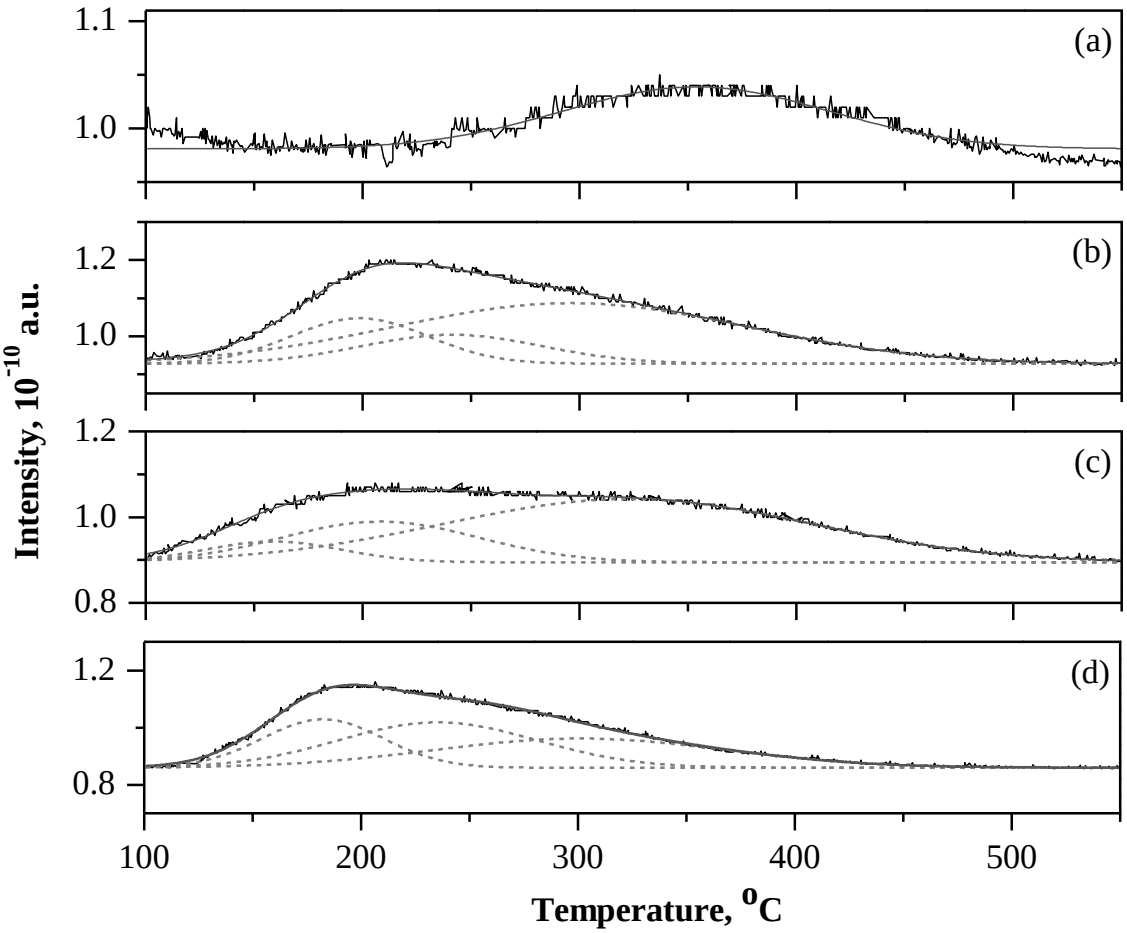

Figure 3 (Supplementary information)

NH_3-TPD profiles of (a) MCM-41 support, (b) 10(Cu)/MCM-41, (c) 10(Fe)/MCM-41, (d) 10(Fe)-10(Cu)/MCM-41 catalysts.

NH_3-TPD profile (experiment) NH_3-TPD profile (program)

Deconvoluted profile of NH_3 desorption

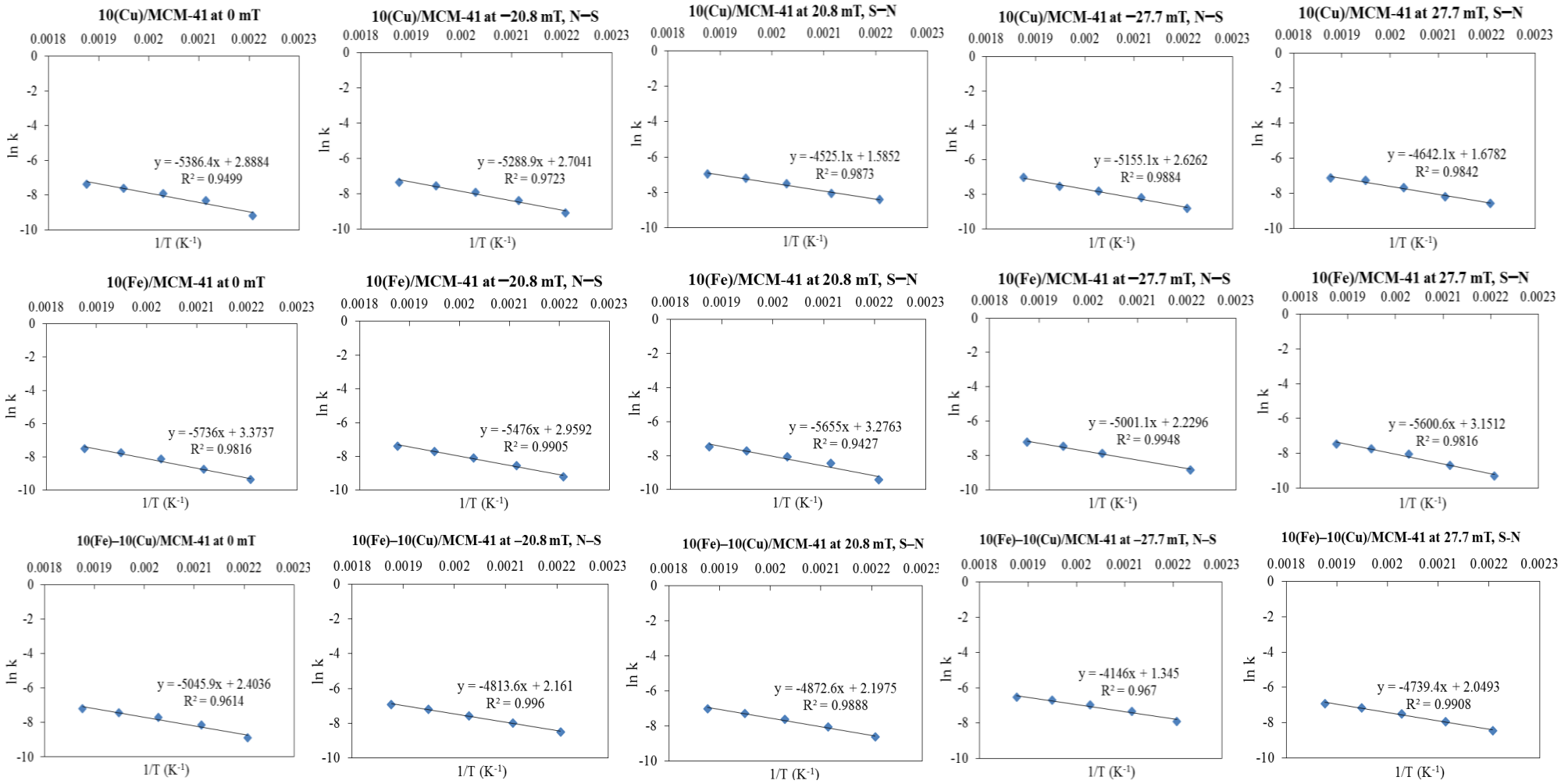

Figure 4 (Supplementary information)

Diagrams of ln (*k*) versus 1/*T* for the activation energy calculation.

Table 1 (Supplementary information)

The magnetic flux density, mT within the reactor measured in radial and axial directions by Tesla meter.

Axial direction, cm	Radial direction, cm				Percentage difference
	0.00	0.30	0.60	0.90	
0.00	–2.564	–2.559	–2.546	–2.563	0.71
0.05	–3.360	–3.385	–3.352	–3.384	0.98
0.10	–4.279	–4.267	–4.250	–4.258	0.68
0.15	–5.049	–5.064	–5.077	–5.082	0.65
0.20	–6.661	–6.642	–6.680	–6.690	0.72
0.25	–7.330	–7.397	–7.354	–7.383	0.91
0.30	–8.279	–8.267	–8.320	–8.258	0.75
0.35	–9.764	–9.759	–9.826	–9.763	0.69
0.40	–10.982	–10.993	–11.012	–11.041	0.54
0.45	–11.968	–12.007	–12.013	–12.031	0.53
0.50	–12.951	–12.995	–13.016	–13.062	0.86
0.55	–13.954	–13.944	–13.987	–14.040	0.69
0.60	–14.305	–14.391	–14.339	–14.358	0.60
0.65	–14.926	–14.902	–15.038	–15.033	0.91
0.70	–15.230	–15.297	–15.214	–15.283	0.55
0.75	–15.527	–15.583	–15.680	–15.620	0.99
0.80	–15.730	–15.775	–15.849	–15.780	0.76
0.85	–15.967	–15.998	–15.953	–16.029	0.48
0.90	–15.951	–15.969	–16.003	–16.046	0.60
0.95	–16.003	–16.008	–16.019	–16.033	0.19
1.00	–16.037	–16.030	–16.021	–16.009	0.17
1.05	–16.070	–16.052	–16.026	–15.989	0.51
1.10	–16.114	–16.085	–16.043	–15.987	0.79

Axial direction, cm	Radial direction, cm				Percentage difference
	0.00	0.30	0.60	0.90	
1.25	–16.340	–16.337	–16.271	–16.183	0.97
1.30	–16.441	–16.484	–16.412	–16.323	0.99
1.35	–16.831	–16.862	–16.792	–16.716	0.87
1.40	–17.026	–17.065	–17.003	–16.946	0.70
1.45	–17.324	–17.267	–17.218	–17.178	0.85
1.50	–17.511	–17.455	–17.417	–17.395	0.67
1.55	–17.671	–17.622	–17.596	–17.590	0.46
1.60	–17.793	–17.752	–17.736	–17.748	0.32
1.65	–17.871	–17.838	–17.830	–17.855	0.23
1.70	–17.900	–17.868	–17.870	–17.905	0.21
1.75	–17.868	–17.841	–17.847	–17.890	0.27
1.80	–17.776	–17.751	–17.760	–17.807	0.32
1.85	–17.620	–17.597	–17.608	–17.654	0.32
1.90	–17.402	–17.380	–17.390	–17.433	0.30
1.95	–17.127	–17.106	–17.113	–17.148	0.25
2.00	–16.800	–16.778	–16.780	–16.806	0.17
2.05	–16.429	–16.406	–16.402	–16.417	0.16
2.10	–16.024	–16.003	–15.994	–15.991	0.21
2.15	–15.595	–15.569	–15.552	–15.540	0.35
2.20	–15.161	–15.135	–15.109	–15.082	0.52
2.25	–14.722	–14.694	–14.662	–14.622	0.68
2.30	–14.176	–14.225	–14.262	–14.290	0.80
2.35	–13.764	–13.823	–13.865	–13.889	0.91
2.40	–13.519	–13.494	–13.451	–13.389	0.97
2.45	–13.184	–13.163	–13.121	–13.056	0.98
2.50	–12.896	–12.878	–12.840	–12.777	0.93
2.55	–12.649	–12.637	–12.602	–12.545	0.83

Axial direction, cm	Radial direction, cm				Percentage difference
	0.00	0.30	0.60	0.90	
2.70	–12.213	–12.248	–12.263	–12.261	0.41
2.75	–12.085	–12.123	–12.144	–12.147	0.51
2.80	–11.985	–12.034	–12.053	–12.069	0.70
2.85	–11.938	–11.974	–12.001	–12.018	0.67
2.90	–11.999	–11.935	–11.964	–12.018	0.70
2.95	–11.878	–11.911	–11.941	–11.967	0.75
3.00	–11.859	–11.889	–11.922	–11.952	0.78
3.05	–11.842	–11.869	–11.902	–11.935	0.79
3.10	–11.814	–11.841	–11.872	–11.907	0.79
3.15	–11.775	–11.801	–11.832	–11.867	0.78
3.20	–11.719	–11.742	–11.771	–11.807	0.75
3.25	–11.644	–11.668	–11.697	–11.730	0.74
3.30	–11.549	–11.575	–11.602	–11.633	0.73
3.35	–11.441	–11.466	–11.494	–11.522	0.71
3.40	–11.315	–11.342	–11.369	–11.394	0.70
3.45	–11.177	–11.206	–11.233	–11.256	0.71
3.50	–11.037	–11.070	–11.097	–11.116	0.72
3.55	–10.898	–10.934	–10.961	–10.980	0.75
3.60	–10.766	–10.804	–10.833	–10.850	0.78
3.65	–10.647	–10.688	–10.719	–10.736	0.84
3.70	–10.544	–10.589	–10.621	–10.640	0.91
3.75	–10.461	–10.508	–10.542	–10.564	0.98
3.80	–10.400	–10.447	–10.485	–10.411	0.82
3.85	–10.459	–10.407	–10.447	–10.478	0.68
3.90	–10.334	–10.379	–10.423	–10.362	0.86
3.95	–10.320	–10.364	–10.410	–10.356	0.87
4.00	–10.303	–10.343	–10.392	–10.349	0.86

Axial direction, cm	Radial direction, cm				Percentage difference
	0.00	0.30	0.60	0.90	
4.15	–10.161	–10.128	–10.129	–10.167	0.39
4.20	–10.004	–9.946	–9.934	–9.966	0.70
4.25	–9.661	–9.680	–9.652	–9.677	0.29
4.30	–9.419	–9.413	–9.471	–9.490	0.82
4.35	–8.945	–8.922	–8.970	–8.972	0.56
4.40	–8.351	–8.300	–8.326	–8.330	0.61
4.45	–7.397	–7.333	–7.345	–7.334	0.87
4.50	–6.676	–6.693	–6.692	–6.675	0.27
4.55	–5.252	–5.221	–5.248	–5.257	0.69
4.60	–4.024	–4.019	–3.997	–3.987	0.93
4.65	–2.584	–2.589	–2.573	–2.565	0.94
4.70	–1.002	–1.003	–0.996	–0.999	0.70
4.75	0.727	0.724	0.725	0.729	–0.69
4.80	2.608	2.613	2.609	2.620	–0.46
4.85	4.489	4.461	4.463	4.446	–0.96
4.90	6.332	6.366	6.378	6.369	–0.72
4.95	8.515	8.510	8.504	8.500	–0.18
5.00	10.598	10.599	10.686	10.680	–0.82
5.05	12.574	12.610	12.581	12.575	–0.29
5.10	14.602	14.604	14.652	14.645	–0.34
5.15	16.514	16.494	16.528	16.616	–0.73
5.20	18.318	18.265	18.285	18.364	–0.54
5.25	20.000	19.921	19.926	20.002	–0.40
5.30	21.511	21.420	21.411	21.477	–0.46
5.35	22.853	22.754	22.730	22.788	–0.54
5.40	23.830	23.766	23.782	23.875	–0.46

Axial direction, cm	Radial direction, cm				Percentage difference
	0.00	0.30	0.60	0.90	
5.55	26.406	26.322	26.314	26.383	–0.35
5.60	26.956	26.867	26.851	26.906	–0.39
5.65	27.361	27.264	27.238	27.284	–0.45
5.70	27.650	27.659	27.741	27.899	–0.89
5.75	27.711	27.727	27.819	27.983	–0.97
5.80	27.633	27.660	27.760	27.734	–0.46
5.85	27.469	27.489	27.563	27.452	–0.40
5.90	27.256	27.249	27.222	27.222	–0.12
5.95	26.536	26.539	26.527	26.544	–0.06
6.00	25.976	25.938	26.091	26.020	–0.59
6.05	25.363	25.238	25.300	25.348	–0.49
6.10	24.085	24.170	24.143	24.098	–0.35
6.15	23.136	23.128	23.208	23.357	–0.98
6.20	21.852	21.852	21.929	21.807	–0.56
6.25	20.572	20.581	20.471	20.544	–0.53
6.30	16.925	16.930	17.007	17.043	–0.69
6.35	14.942	15.052	15.016	15.034	–0.73
6.40	12.996	13.100	13.043	13.023	–0.79
6.45	10.993	11.001	11.009	11.065	–0.65
6.50	8.996	9.007	9.007	9.012	–0.18
6.55	6.970	6.989	7.024	7.007	–0.77
6.60	4.937	4.944	4.955	4.980	–0.86
6.65	2.929	2.916	2.938	2.919	–0.75
6.70	0.997	1.001	1.005	0.998	–0.80
6.75	–0.725	–0.720	–0.724	–0.727	0.97
6.80	–2.399	–2.377	–2.399	–2.383	0.93
6.85	–3.888	–3.858	–3.868	–3.851	0.96

Axial direction, cm	Radial direction, cm				Percentage difference
	0.00	0.30	0.60	0.90	
7.00	–7.282	–7.276	–7.256	–7.224	0.80
7.05	–8.109	–8.066	–8.095	–8.120	0.67
7.10	–8.754	–8.782	–8.752	–8.776	0.34
7.15	–9.252	–9.220	–9.266	–9.288	0.74
7.20	–9.617	–9.669	–9.646	–9.663	0.54
7.25	–9.859	–9.848	–9.898	–9.901	0.54
7.30	–9.998	–9.993	–10.041	–10.050	0.57
7.35	–10.047	–10.050	–10.099	–10.092	0.52
7.40	–10.027	–10.038	–10.084	–10.069	0.57
7.45	–10.047	–10.050	–10.099	–10.092	0.52
7.50	–10.027	–10.038	–10.084	–10.069	0.57
7.55	–10.047	–10.050	–10.099	–10.092	0.52
7.60	–10.027	–10.038	–10.084	–10.069	0.57
7.65	–10.047	–10.050	–10.099	–10.092	0.52
7.70	–10.027	–10.038	–10.084	–10.069	0.57
7.75	–10.047	–10.050	–10.099	–10.092	0.52
7.80	–10.027	–10.038	–10.084	–10.069	0.57
7.85	–10.047	–10.050	–10.099	–10.092	0.52
7.90	–10.027	–10.038	–10.084	–10.069	0.57
7.95	–10.047	–10.050	–10.099	–10.092	0.52
8.00	–10.027	–10.038	–10.084	–10.069	0.57
8.05	–10.047	–10.050	–10.099	–10.092	0.52
8.10	–10.027	–10.038	–10.084	–10.069	0.57
8.15	–10.047	–10.050	–10.099	–10.092	0.52
8.20	–10.027	–10.038	–10.084	–10.069	0.57
8.25	–10.033	–10.069	–10.110	–10.054	0.77
8.30	–10.108	–10.143	–10.180	–10.155	0.71

Axial direction, cm	Radial direction, cm				Percentage difference
	0.00	0.30	0.60	0.90	
8.45	–10.319	–10.346	–10.375	–10.408	0.86
8.50	–10.352	–10.375	–10.398	–10.422	0.68
8.55	–10.387	–10.407	–10.424	–10.437	0.48
8.60	–10.430	–10.447	–10.456	–10.459	0.28
8.65	–10.490	–10.504	–10.507	–10.498	0.16
8.70	–10.577	–10.588	–10.584	–10.565	0.22
8.75	–10.694	–10.704	–10.695	–10.666	0.36
8.80	–10.849	–10.862	–10.852	–10.815	0.43
8.85	–11.056	–11.066	–11.051	–11.012	0.49
8.90	–11.304	–11.313	–11.304	–11.263	0.44
8.95	–11.603	–11.614	–11.602	–11.570	0.38
9.00	–11.942	–11.957	–11.958	–11.928	0.25
9.05	–12.324	–12.344	–12.345	–12.328	0.17
9.10	–12.746	–12.767	–12.780	–12.780	0.27
9.15	–13.176	–13.204	–13.218	–13.240	0.49
9.20	–13.735	–13.703	–13.670	–13.634	0.74
9.25	–14.225	–14.176	–14.132	–14.088	0.97
9.30	–14.514	–14.647	–14.588	–14.539	0.92
9.35	–15.101	–15.108	–15.042	–14.986	0.81
9.40	–15.499	–15.462	–15.539	–15.534	0.50
9.45	–15.979	–15.943	–15.927	–16.032	0.66
9.50	–16.123	–16.191	–16.120	–16.198	0.48
9.55	–16.523	–16.497	–16.591	–16.508	0.57
9.60	–16.678	–16.750	–16.647	–16.765	0.71
9.65	–16.968	–16.989	–17.092	–17.016	0.73
9.70	–17.082	–17.157	–17.251	–17.163	0.99
9.75	–17.223	–17.294	–17.382	–17.288	0.92

Axial direction, cm	Radial direction, cm				Percentage difference
	0.00	0.30	0.60	0.90	
9.90	–17.598	–17.551	–17.609	–17.669	0.67
9.95	–17.569	–17.614	–17.658	–17.700	0.75
10.00	–17.644	–17.681	–17.712	–17.735	0.52
10.05	–17.734	–17.763	–17.779	–17.787	0.30
10.10	–17.826	–17.853	–17.866	–17.866	0.22
10.15	–17.961	–17.979	–17.985	–17.975	0.13
10.20	–18.117	–18.127	–18.126	–18.108	0.10
10.25	–18.294	–18.297	–18.291	–18.273	0.13
10.30	–18.487	–18.485	–18.477	–18.458	0.16
10.35	–18.683	–18.678	–18.669	–18.660	0.12
10.40	–18.883	–18.873	–18.873	–18.869	0.07
10.45	–19.054	–19.044	–19.049	–19.062	0.09
10.50	–19.200	–19.187	–19.199	–19.231	0.23
10.55	–19.286	–19.278	–19.301	–19.356	0.40
10.60	–19.305	–19.299	–19.337	–19.416	0.61
10.65	–19.240	–19.236	–19.294	–19.395	0.83
10.70	–19.060	–19.069	–19.122	–19.073	0.33
10.75	–18.773	–18.787	–18.804	–18.821	0.26
10.80	–18.633	–18.646	–18.651	–18.637	0.10
10.85	–17.964	–17.994	–17.990	–18.094	0.72
10.90	–16.991	–17.032	–17.049	–17.061	0.41
10.95	–16.375	–16.320	–16.340	–16.469	0.91
11.00	–15.495	–15.444	–15.483	–15.441	0.35
11.05	–13.582	–13.543	–13.596	–13.549	0.39
11.10	–12.199	–12.174	–12.129	–12.201	0.59
11.15	–10.439	–10.522	–10.457	–10.517	0.80
11.20	–8.677	–8.659	–8.689	–8.612	0.89
11.35	–2.850	–2.851	–2.859	–2.857	0.32
11.40	–0.868	–0.867	–0.860	–0.861	0.93